8-1-2017

Secular Resonances during Main-Sequence and Post-Main-Sequence Planetary System Dynamics

Jeremy L. Smallwood
University of Nevada, Las Vegas

SECULAR RESONANCES DURING MAIN-SEQUENCE AND POST-MAIN-SEQUENCE PLANETARY SYSTEM DYNAMICS

By

Jeremy L. Smallwood

Bachelor of Science – Astrophysics
Baylor University
2015

A thesis submitted in partial fulfillment
of the requirements for the

Master of Science – Astronomy

Department of Physics and Astronomy
College of Sciences
The Graduate College

University of Nevada, Las Vegas
August 2017

UNLV | GRADUATE COLLEGE

Thesis Approval

The Graduate College
The University of Nevada, Las Vegas

June 13, 2017

This thesis prepared by

Jeremy L. Smallwood

entitled

Secular Resonances during Main-Sequence and Post-Main-Sequence Planetary System Dynamics

is approved in partial fulfillment of the requirements for the degree of

Master of Science – Astronomy
Department of Physics and Astronomy

Rebecca Martin, Ph.D.
Examination Committee Chair

Kathryn Hausbeck Korgan, Ph.D.
Graduate College Interim Dean

Stephen Lepp, Ph.D.
Examination Committee Member

George Rhee, Ph.D.
Examination Committee Member

Arya Udry, Ph.D.
Graduate College Faculty Representative

ABSTRACT

We investigate gravitational perturbations of an asteroid belt by secular resonances. We apply analytic and numerical models to main–sequence and post–main–sequence planetary systems. First, we investigate how the asteroid impact rate on the Earth is affected by the architecture of the planetary system. We find that the ν_6 resonance plays an important role in the asteroid collision rate with the Earth. Compared to exoplanetary systems, the solar system is somewhat special in its lack of a super–Earth mass planet in the inner solar system. We therefore consider the effects of the presence of a super–Earth in the terrestrial planet region. We find a significant effect for super–Earths with a mass of around $10\,\mathrm{M}_\oplus$ and a separation greater than about $0.7\,\mathrm{AU}$. These results have implications for the habitability of exoplanetary systems. Secondly, we model white dwarf pollution by asteroids from secular resonances. In the past few decades, observations have revealed signatures of metals polluting the atmospheres of white dwarfs that require a continuous accretion of asteroids. We show that secular resonances driven by two outer companions can provide a source of pollution if an inner terrestrial planet is engulfed during the red-giant branch phase. Secular resonances may be a viable mechanism for the pollution of white dwarfs in a variety of exoplanetary system architectures including systems with two giant planets and systems with one giant planet and a binary star companion.

ACKNOWLEDGEMENTS

All the simulations ran at the UNLV National Supercomputing Institute on the Cherry Creek cluster. This research made use of the Exoplanet Orbit Database and the Exoplanet Data Explorer at exoplanets.org.

TABLE OF CONTENTS

LIST OF FIGURES

CHAPTER 1

INTRODUCTION

Resonances shape the architecture within a solar system, which plays an important role in the evolution of that system. In general, a resonance arises when two periods or frequencies are in a simple numerical ratio. There are two types of resonances that can occur, a mean-motion resonance and a secular resonance. Each of these resonances occurs between two objects orbiting a central body. In our solar system, many asteroids are located in the asteroid belt between Mars and Jupiter. Over time, some asteroids undergo resonant gravitational perturbations from the two largest planets, Jupiter and Saturn, causing the asteroids to become scattered from the asteroid belt (Morbidelli et al. 1995; Gladman et al. 1997; Morbidelli & Gladman 1998; Bottke et al. 2000; Petit et al. 2001; Ito & Malhotra 2006; Brož & Vokrouhlický 2008; Minton & Malhotra 2010; Chrenko et al. 2015; Granvik et al. 2017). In a mean-motion resonance, the ratio of the orbital periods of two objects is an integer ratio (e.g. Armitage 2013). Secular resonances arise when the apsidal or nodal precession rates of two objects orbiting a central object are close (Froeschle & Scholl 1986; Yoshikawa 1987).

The most prevalent secular resonance in our solar system in the ν_6 resonance (Ito & Malhotra 2006; Minton & Malhotra 2011), which occurs between the apsidal precession of the asteroids and Saturn. The outer edge of the ν_6 resonance sets the inner boundary for our asteroid belt, which is approximately located at $2\,\mathrm{AU}$. A large fraction of near Earth asteroids originate from the inner main belt rather than the middle or outer belt (Bottke et al. 2002). Many of these asteroids within

the inner main belt are injected in the ν_6 resonance and end up reaching Earth-crossing orbits (Morbidelli et al. 1994; Bottke et al. 2000).

When asteroids encounter a resonance, their eccentricities can be increased to a point where they are either ejected from the system or collide with a planet or the central star. Each resonance has a width, in semi-major axis, over which it operates (Dermott & Murray 1983). Asteroids that fall within this width undergo perturbations causing their eccentricities to increase. Regions in which the widths overlap are known as chaotic regions (Murray & Holman 1997; 1999), and there almost all of the asteroids are cleared out. The region where Jupiter's mean-motion resonances overlap is what determines the outer edge of the asteroid belt at about $3.3\,\mathrm{AU} \sim 3.5\,\mathrm{AU}$.

When asteroids encounter a resonance, their eccentricities are increased to a point where they are either ejected from the system or collide with a planet or the central star. These perturbations begin about 10^6 years after the disk is dispersed (Morbidelli et al. 1994; Ito & Tanikawa 1999).

Asteroid Impacts on Terrestrial Planets

Asteroidal impacts on terrestrial planets may be important for planet habitability. Water must have been delivered to the surface of the Earth, potentially through asteroid impacts (Morbidelli et al. 2000; Raymond et al. 2007), even though comet collisions and the interaction between the magma and atmosphere have also been suggested as sources of the planet's water (Genda & Ikoma 2008). Large moons may be produced through asteroid collisions (Canup & Asphaug 2001; Canup 2012). Our Moon plays an intricate role in the Earth's habitability by stabilizing the rotation axis of the Earth, preventing weather extremes due to chaotic motion. According to some hypotheses, life itself may have been delivered to Earth by asteroids (Cronin & Pizzarello 1983; Castillo-Rogez

et al. 2008; Houtkooper 2011). Important heavy elements needed for the existence of life may have also been delivered by asteroid impacts (Willbold et al. 2011). The *rate* of asteroid impacts also can have a significant effect on a planet's habitability. A high rate of impacts could have led to a highly cratered planet, not hospitable to life. On the other hand, too few impacts could suppress the delivery of essential elements. The evolution of life on Earth shows that the presence of an asteroid belt could be necessary (e.g. through mass extinctions) even for the appearance of complex life and intelligence in an exosolar planetary system.

Asteroid belts, if they form at all, form most likely interior to giant planets (Morales et al. 2011; Martin & Livio 2013). This coincides with the location of the water snow line, the radius outside of which water is found in a solid form (Lecar et al. 2006). Giant planets form outside of the snow line and the terrestrial planets form inward of it (Raymond et al. 2009). While the gas disk is present, the eccentricities and inclinations of asteroids are damped by tidal interactions with the protoplanetary gas disk (Ward 1989; 1993; Artymowicz 1993; Agnor & Ward 2002; Kominami & Ida 2002). The lifetime of the gas disk is typically a few million years (Haisch et al. 2001), after which photoevaporation disperses the disk. A pressure gradient arises when stellar radiation heats the disk, allowing the thermal energy of the gas to exceed its gravitational binding energy (Alexander et al. 2006; Armitage 2013). Once the gas disk is removed, gravitational perturbations cause a clearing of asteroids at many resonances locations (Morbidelli et al. 1995; Gladman et al. 1997; Morbidelli & Gladman 1998; Petit et al. 2001; Brož & Vokrouhlický 2008; Minton & Malhotra 2010; Chrenko et al. 2015) leading to the formation of potential Earth impactors (Morbidelli & Nesvorný 1999; Strom et al. 2005).

Since Jupiter and Saturn are the largest planets in the solar system, they are the main driving force for the dynamic evolution of the asteroid belt. The effect that Jupiter had on the asteroid

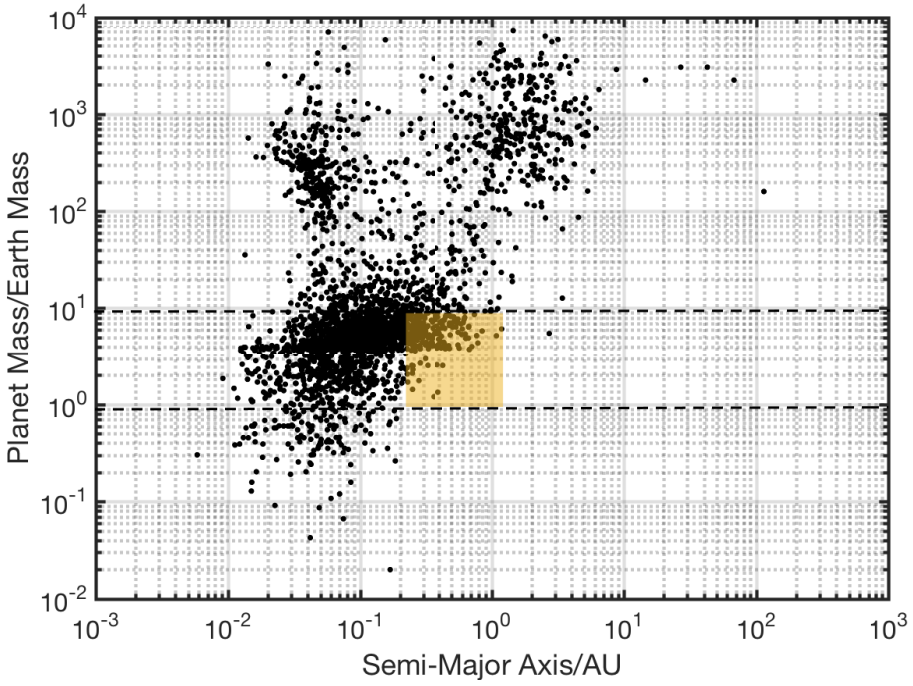

Figure 1.1: Planet mass and semi-major axis of observed exoplanets. The area between the two black-dotted lines contains the range of super-Earth masses ($1\,\mathrm{M}_\oplus < \mathrm{M_p} < 10\,\mathrm{M}_\oplus$) used in simulations described in Section 2. The transparent yellow box denotes the observed super-Earths with a semi-major axis in the inner solar system. The data are from exoplanets.org (Han et al. 2014).

collision rate on the Earth is debated (Horner & Jones 2008; 2012). The asteroid belt we observe today is roughly 0.1% in mass of the original asteroid belt formed in the beginning of the solar system. Several of the well known mean-motion resonances in our solar system are the Kirkwood gaps (Dermott & Murray 1983; Moons 1996; Vrbik 1996; O'Brien et al. 2007), which are found within the asteroid belt.

The outer edge of the ν_6 resonance sets the inner boundary for our asteroid belt, which is approximately located at $2\,\mathrm{AU}$. A large fraction of near Earth asteroids originate from the inner main belt rather than the middle or outer belt (Bottke et al. 2002). Many of these asteroids within the inner main belt are injected in the ν_6 resonance and end up reaching Earth-crossing orbits (Morbidelli et al. 1994; Bottke et al. 2000).

The importance of the ν_6 resonance is apparent through observations of craters in the solar system. The Late Heavy Bombardment (LHB) event occurred early in the evolution of the solar system. During this period, many lunar craters were formed from a large barrage of comets and asteroids. The LHM is assumed to have ended about 3.7 to 3.8 billion years ago. Bottke et al. (2012) found that the majority of these asteroids originated from the hypothetical extension of the asteroid belt, the E-belt, which was located between 1.7 and $2.1\,\mathrm{AU}$. This region underwent instabilities due to giant planet migration and is now currently depleted except for a family of high inclination asteroids.

Observations of exoplanetary systems show an abundance of systems that possess a super-Earth (Borucki et al. 2010; 2011; Batalha et al. 2013), a planet with a mass in the range of $1 - 10M_{\oplus}$ (Valencia et al. 2007). Fig. 1.1 shows the planet mass and semi–major axis of observed exoplanets. The area between the two black–dotted lines contains the observed super–Earths. The transparent yellow box denotes the observed super–Earths with a semi-major axis located at orbital radii in the range of the terrestrial planets in the solar system. The vast majority of observed super–Earths are close to their parent star, although this is most likely a selection effect (Chiang & Laughlin 2013). In a recent work, Martin & Livio (2015) have shown that perhaps the main characteristic that distinguishes the solar system from the observed exoplanetary systems is the absence of super–Earths. Consequently, it is very interesting to examine the effects that the presence of a super–Earth would have had on asteroid impacts on Earth. Since the evolution of a planetary system is a chaotic process (Malhotra 1999), adding a super-Earth can greatly influence the architecture of an exoplanetary system. There are likely additional mechanisms that operate in exoplanetary systems that result in the migration of planets, through the gas disk (Armitage 2013), through the planetesimal disk (Wyatt 2003; Gomes et al. 2004), via secular processes such as the Kozai–Lidov

mechanism (Kozai 1962; Lidov 1962; Wu & Murray 2003; Takeda & Rasio 2005; Martin et al. 2016) and through planet–planet scattering (Ford & Rasio 2008; Dawson & Murray-Clay 2013). The Kepler data suggest that there is a overabundance of planetary systems with only one planet (Lissauer et al. 2011; Hansen & Murray 2013) and this may be due to the destructive motion of the planet (e.g. Morton & Winn 2014).

In this work we are interested in multi–planet exoplanetary systems in which there has not been violent processes that might have destroyed an asteroid belt and prevented the formation of terrestrial planets early in the lifetime of the system. Specifically, we investigate how the architecture of the solar system affects asteroid impacts on the Earth.

White Dwarf Pollution

About 30% to 50% of all white dwarfs have metal-polluted atmospheres identified by metallic absorption lines from spectroscopic measurements (e.g. Cottrell & Greenstein 1980; Koester et al. 1982; Lacombe et al. 1983; Zeidler-K.T. et al. 1986; Koester et al. 1997; Zuckerman et al. 2003; Klein et al. 2010; Vennes et al. 2010; Zuckerman et al. 2010; Melis & Dufour 2017). A total of about 1000 white dwarfs are known to be polluted. These findings appear at first glance to be puzzling since white dwarf atmospheres stratify chemical elements through gravitational settling (Koester & Wilken 2006; Koester 2009). The stratification or diffusion timescales for metals are of the order of days to weeks for DA (hydrogen atmosphere) white dwarfs and $10^4 - 10^6$ yrs for DB (helium atmosphere) white dwarfs (Koester & Wilken 2006). This implies that the diffusion timescale of metals is many orders of magnitude shorter than the white dwarf cooling time (Paquette et al. 1986). Once the white dwarf has cooled below $25,000\,\mathrm{K}$, metals are no longer supported

by radiative forces and rapidly sink and diffuse within the white dwarf's atmosphere due to the intense gravity environment (Fontaine & Michaud 1979; Vauclair et al. 1979; Koester 2009). It takes about $20\,\mathrm{Myr}$ to reach a temperature of $25,000\,\mathrm{K}$ (Fontaine et al. 2001). It is noteworthy that DA white dwarfs fall in a temperature range from $25,000$ K to $5,000$ K, which coincides with cooling ages of $2\,\mathrm{Gyr}$ to $20\,\mathrm{Myr}$, respectively (Koester et al. 2014). Accretion disks and pollution are observed at $30\,\mathrm{Myr}$ to $600\,\mathrm{Myr}$ cooling ages (Farihi 2016). Thus, these polluted white dwarfs need to be continuously accreting metal-rich material in order to observe the metal absorption lines.

Several theoretical models have been explored to explain the metal pollution. Accretion of metallic material originating from the interstellar medium has been conclusively ruled out by Farihi et al. (2010a) (see also Aannestad et al. 1993; Jura 2006; Kilic & Redfield 2007; Barstow et al. 2014). The currently favored pollution mechanism suggests that metal-rich planetary material is tidally disrupted into a debris disk and then subsequently accreted onto the white dwarf (Gänsicke et al. 2006; Kilic et al. 2006; von Hippel et al. 2007; Farihi et al. 2009; Jura et al. 2009; Farihi et al. 2010b; Melis et al. 2010; Brown et al. 2017)(See also Farihi 2016; for review). The sources of pollution that have been proposed include asteroids (Jura 2003; 2006; Jura et al. 2009; Debes et al. 2012), comets (Caiazzo & Heyl 2017), moons via planet-planet scattering (Payne et al. 2016; 2017) and perturbations of planetary material due to eccentric planets (Frewen & Hansen 2014). Perturbations may be also caused by Kozai-Lidov instabilities in stellar binaries (Hamers & Portegies Zwart 2016; Petrovich & Muñoz 2017).

The chain of events is thought to be as follows. As a main-sequence star evolves, the star undergoes significant mass loss during the red-giant branch (RGB) phase (Reimers 1977; McDonald & Zijlstra 2015) and during the asymptotic giant branch (AGB) phase (Rosenfield et al. 2014; 2016). This mass loss is a result of radiation pressure pushing on the loosely bound outer layers

of the red giant. The mass outflow, or stellar wind, leads to mass-loss rates of up to $10^{-4}\,\mathrm{M}_{\odot}\mathrm{yr}^{-1}$ (e.g. Maoz 2016) that depletes the star of a large fraction of its initial mass. During the expansion of the outer envelop, close-in planets are engulfed (Siess & Livio 1999; Villaver & Livio 2007; 2009; Mustill & Villaver 2012; Adams & Bloch 2013; Villaver et al. 2014), leading (among other things) to dynamical changes within the system. As the star undergoes significant mass loss, due to conservation of angular momentum, the orbits of all surviving bodies expand outward (Duncan & Lissauer 1998). For planets and asteroids that are at orbital radii $a_{\mathrm{p}} \lesssim 2000\,\mathrm{AU}$, the timescale for mass loss is shorter than the orbital periods of the planets and so the orbits of the planets and asteroids expand adiabatically (Veras et al. 2013; Caiazzo & Heyl 2017).

Debes et al. (2012) investigated white dwarf pollution by asteroids that originate from the 2:1 mean-motion resonance with Jupiter. In their model, as the star loses mass through its stellar evolution, the libration width of the 2:1 resonance is slightly widened, forcing previously stable asteroids to eventually become accreted onto the white dwarf. We propose that secular resonances may provide an additional mechanism and source of pollution. Because of the changing planetary dynamics in the system, the location of secular resonances does not necessarily change adiabatically as do mean-motion resonances. For example, in our solar system, the ν_6 resonance has a smaller orbital radius than the 2:1 resonance, which may allow a greater number of asteroids from the ν_6 resonance to become tidally disrupted by the white dwarf.

In the present work we investigate the evolution of a system that contains a white dwarf that harbors a planetary system and an exo-asteroid belt. The giant outer planets and the asteroid belt are sufficiently far from the white dwarf that they survive the stellar evolution through the RGB/AGB phases. We consider systems with two giant planets, like the solar system, and systems with one giant planet and a binary stellar companion. We explore how different system architectures are

able to pollute the atmospheres of white dwarfs.

CHAPTER 2

ANALYTICAL MODELS

Eigenfrequency

The ν_6 secular resonance properties are affected by both Saturn and Jupiter (Bottke et al. 2000; Ito & Malhotra 2006). Jupiter increases the precession frequency of the asteroids so that they fall into a resonance with the apsidal precession rate of Saturn. The location of the ν_6 resonance is found by calculating the location of intersection of a test particle's precession rate with Saturn's eigenfrequency. We consider a planetary system with a total of N planets orbiting a central object with mass m_*. Each planet has a semi–major axis a_j, mass m_j and orbital frequency $n_j = \sqrt{Gm_*/a_j^3}$, where $j = 1, ..., N$. The eigenfrequency of each planet is found by calculating the eigenvalues of the $N \times N$ matrix A_{jk} associated with a generalized form of the secular perturbation theory

$$A_{jk} = -\frac{1}{4}\frac{m_k}{m_* + m_j} n_j \alpha_{jk} \bar{\alpha}_{jk} b^{(2)}_{3/2}(\alpha_{jk}) \tag{2.1}$$

for $j \neq k$ and otherwise

$$A_{jj} = \frac{1}{4} \sum_{k=1, k\neq j}^{N} \frac{m_k}{m_* + m_j} \alpha_{jk} \bar{\alpha}_{jk} b^{(1)}_{3/2}(\alpha_{jk}) \tag{2.2}$$

(Murray & Dermott 2000; Minton & Malhotra 2011; Malhotra 2012), where the Laplace coefficient $b_s^{(j)}(\alpha)$ is given by

$$\frac{1}{2}b_s^{(j)}(\alpha) = \frac{1}{2\pi}\int_0^{2\pi} \frac{\cos(j\psi)\, d\psi}{(1 - 2\alpha\cos\psi + \alpha^2)^s} \tag{2.3}$$

and α_{jk} and $\bar{\alpha}_{jk}$ are defined as

$$\alpha_{jk} = \begin{cases} a_k/a_j, & \text{if } a_j > a_k \quad \text{(internal perturber)}, \\ \\ a_j/a_k, & \text{if } a_j < a_k \quad \text{(external perturber)}, \end{cases} \tag{2.4}$$

and

$$\bar{\alpha}_{jk} = \begin{cases} 1, & \text{if } a_j > a_k \quad \text{(internal perturber)}, \\ \\ a_j/a_k, & \text{if } a_j < a_k \quad \text{(external perturber)}. \end{cases} \tag{2.5}$$

We find that the g_6 eigenfrequency has a value of $22.13''\mathrm{yr}^{-1}$ (includes only Jupiter and Saturn) and a value of $22.16''\mathrm{yr}^{-1}$ (includes all the planets in the Solar System), which is lower by roughly 20% from the more accurate value of $27.77''\mathrm{yr}^{-1}$ given by Brouwer & van Woerkom (1950) (See also Minton & Malhotra 2011). Brouwer & van Woerkom (1950) obtained a more accurate value of the eigenfrequency by including higher-order terms in the disturbing function, due to Jupiter and Saturn's proximity to the 5:2 resonance (Minton & Malhotra 2011). Fernandez & Ip (1984) and Fernández & Ip (1996) suggested that the jovian planets proximity to the current near resonant structure could be a consequence of the differential expansion of their orbits during late stages of planetary formation (see also Michtchenko & Ferraz-Mello 2001).

Asteroid Precession Rates

We calculate the precession rate of test particles in the potential of the planetary system. The precession rate is given by

$$\dot{\varpi} = \frac{n}{4} \sum_{j=1}^{N} \frac{m_j}{m_*} \alpha_j \bar{\alpha}_j b_{3/2}^{(1)}(\alpha_j) \tag{2.6}$$

(e.g. Murray & Dermott 2000), where n is the orbital frequency of the test particle. In this work, we take $N = 2$ and consider only the planets Jupiter and Saturn since the inner planets are engulfed during the RGB/AGB phases. The outer giants Neptune and Uranus do not significantly affect the dynamics of the asteroid belt (Izidoro et al. 2016). Saturn also does not noticeably affect the precession rate of the asteroids in the asteroid belt – that rate is dominated by Jupiter.

Resonance Widths

Each mean-motion and secular resonance has a width that the resonant perturbations operate over. Asteroids within this width undergo heightened eccentricities, causing the asteroids to impact a larger body or be ejected from the system. In order to calculate the width of the ν_6 secular resonance, we follow Malhotra (2012) and calculate the maximum forced eccentricity of a test particle near the ν_6 resonance, which is given by

$$e_{\max} = \frac{F_6}{g_0 - g_6}, \tag{2.7}$$

where g_0 is the natural frequency, g_6 is Saturn's secular eigenfrequency, and F_6 represents Saturn's planetary secular mode frequency. The natural frequency and the secular mode frequency are given

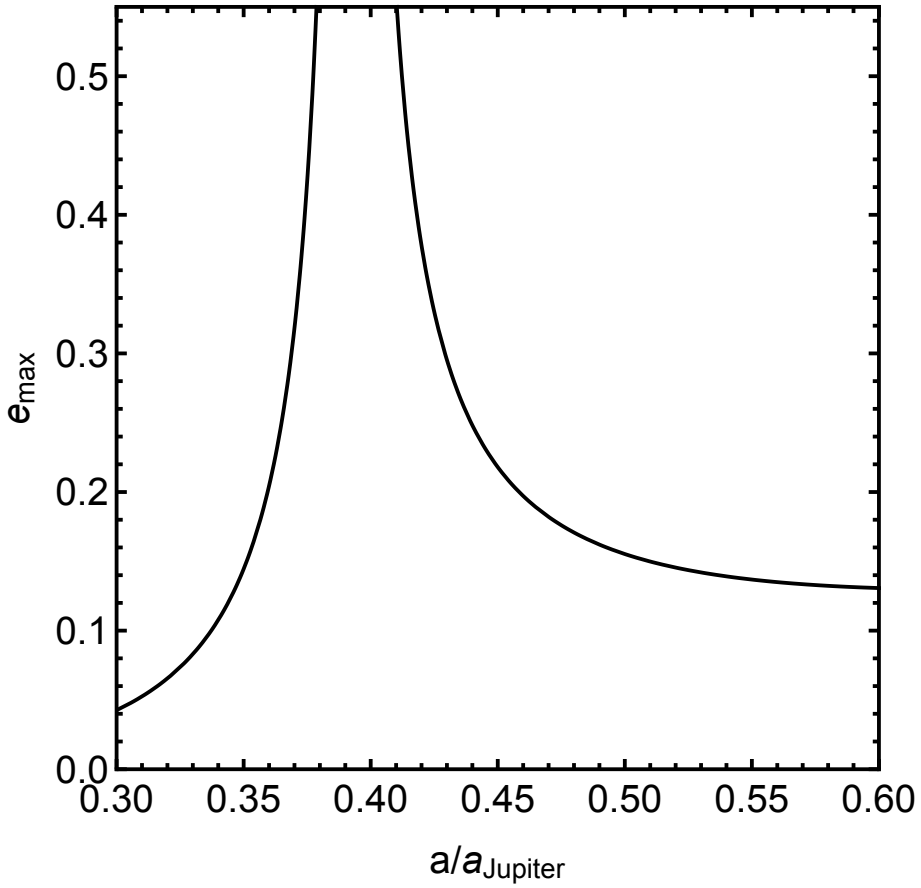

Figure 2.1: Forced eccentricity of a test particle near the ν_6 secular resonance as a function of semi-major axis.

by

$$g_0 = \frac{1}{2}\sum_{j=1}^{N} \frac{m_j\sqrt{a_j}}{m_*\sqrt{a}}\alpha_j\bar{\alpha_j}b_{3/2}^{(1)}(\alpha_j)n_j \tag{2.8}$$

and

$$F_6 = \frac{1}{8}\sum_{j=1}^{N} \frac{m_j\sqrt{a_j}}{m_*\sqrt{a}}\alpha_j\bar{\alpha_j}b_{3/2}^{(2)}(\alpha_j)n_jE_j^{(6)}, \tag{2.9}$$

respectively, where $\alpha_j = \min\{a/a_j, a_j/a\}$, $\bar{\alpha_j} = \min\{1, a/a_j\}$, m_* is the mass of the star, a is the semi-major axis of the test particle and $E_j^{(6)}$ is the component of the eigenvectors related to the 6^{th} secular mode. The values of $E_j^{(6)}$ are determined by calculating the eigenvectors of the matrix A_{ij} given in equations (2.1) and (2.2).

Figure 2.2 is a reconstruction of the liberation widths for the first-order mean-motion resonances with Jupiter. The areas where the liberation widths overlap are known as chaotic regions, where almost all of the asteroids will be cleared out. It is possible to derive analytic estimates of the liberation widths of the resonance. An expression for these widths is given by Dermott & Murray (1983)

$$\frac{\delta a_{max}}{a} = \pm\left(\frac{16}{3}\frac{\mid C_r \mid}{n}\right)^{1/2}\left(1 + \frac{1}{27 j_2^2 e^3}\frac{\mid C_r \mid}{n}\right)^{1/2} - \frac{2}{9 j_2 e}\frac{\mid C_r \mid}{n}, \tag{2.10}$$

where j_2 is a coefficient and C_r is the resonant part of the disturbing function, given by

$$C_r = \left(\frac{m^{'}}{m_c}\right) n \alpha f_d(\alpha). \tag{2.11}$$

Figure 2.3 shows the evolution of an asteroid belt in the presence of a Jupiter-mass planet on a non-inclined circular orbit from time $t = 0\mathrm{Myr}$ to $t = 90\mathrm{Myr}$. The dark transparent regions indicate the libration widths of mean-motion resonances with Jupiter. Initially the asteroids semi-major axes are calculated and binned from a uniform distribution (discussed further in Chapter 3). During the asteroid belt's evolution, asteroids are cleared out at various resonance locations by heightened eccentricities.

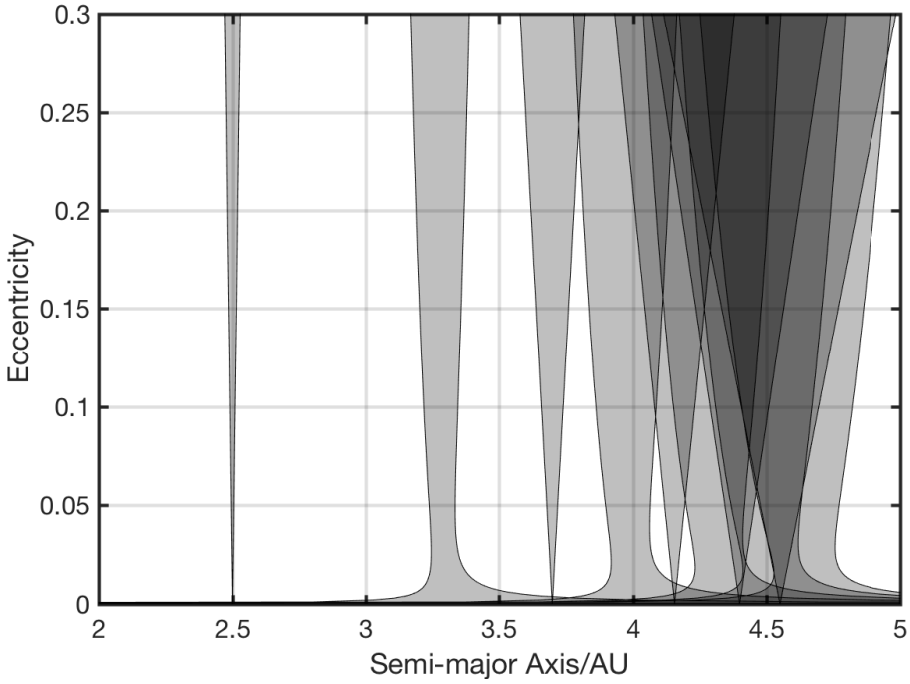

Figure 2.2: The transparent regions represent the libration width as a function of semi-major axis and eccentricity for a selection of Jupiter's mean-motion resonances located within the asteroid belt. The overlapping of the libration widths denotes Jupiter's chaotic region.

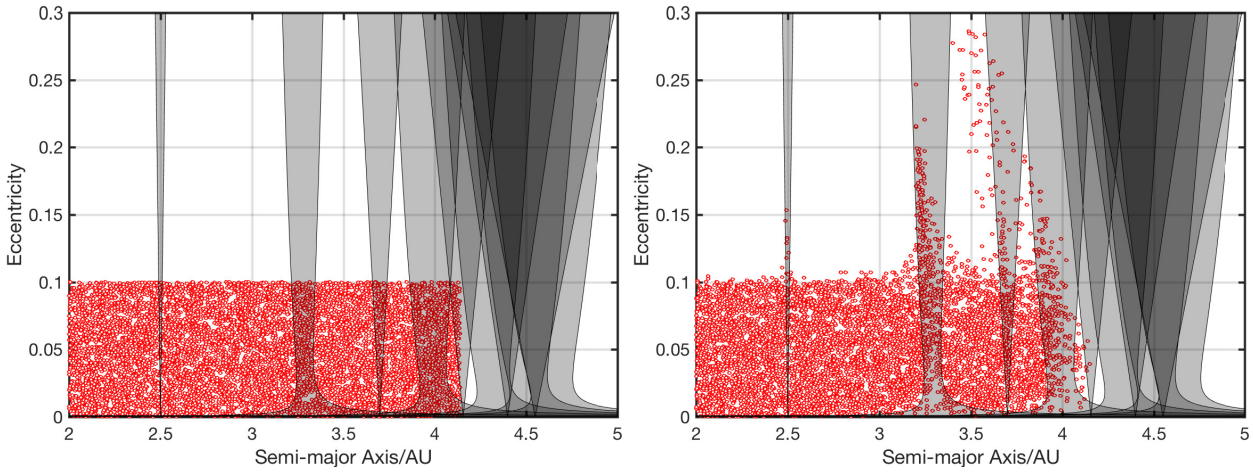

Figure 2.3: The transparent regions represent the libration width as a function of semi-major axis and eccentricity for a selection of Jupiter's mean-motion resonances located within the asteroid belt. The overlapping of the libration widths denotes Jupiter's chaotic region. The red circles represent a single asteroid within our asteroid distribution. Simulation times are shown at $t = 0\text{Myr}$ (left panel) and $t = 90\text{Myr}$ (right panel).

CHAPTER 3

NUMERICAL MODELS

We use the hybrid symplectic integrator in the orbital dynamics package, MERCURY, to model the structure of the asteroid belt and the asteroid impact rate on the Earth in the presence of a super–Earth. MERCURY uses N-body integrations to calculate the orbital evolution of objects moving in the gravitational field of a large body (Chambers 1999).

The asteroids in our simulations are point particles that do not interact gravitationally with one another but do interact gravitationally with the planets and the central object. We may neglect this interaction because the timescale for asteroid-asteroid collisional interaction is much longer than the timescale for the action of perturbations by resonance effects. The timescale for resonant effects is on the order of $\sim 1\,\mathrm{Myr}$ (Ito & Tanikawa 1999), whereas some of the largest asteroids have collisional timescales that are of the order of magnitude of the age of the solar system (Dohnanyi 1969).

The orbit of each asteroid is defined by six orbital elements, a, i, e, n, g and M_{a}. The semi-major axis, a, is distributed uniformly in the range $a_{\min} < a < a_{\max}$, the inclination, i, is randomly allocated from the range $0-10^{\circ}$, the eccentricity, e, is randomly generated from the range $0.0-0.1$. The longitude of the ascending node, n, the argument of perhelion, g, and the mean anomaly, M_a, are all uniformly randomly sampled from the range $0-360^{\circ}$. The longitude of the ascending node, n, is defined as the angle from a reference direction to the ascending node, g is the angle from the ascending node to the object's periastron, and M_{a} is the angular distance from the periastron.

Asteroid Impacts on Terrestrial Planets

We simulate the motion of a super-Earth, Earth, Jupiter, Saturn, and a distribution of asteroids orbiting a central object. The asteroids interact gravitationally with the planets and the star but do not interact with one another. We calculate the evolution of each asteroid orbit for a duration of ten million years.

The total mass observed in the solar system's asteroid belt is about $5 \times 10^{-4} M_{\oplus}$, with about 80% of the mass contained in the three largest asteroids (Ceres, Pallas, and Vesta). Today, there are over $10,000$ asteroids with high accuracy measurements of the semi-major axis, with the mean being $< a >= 2.74 \pm 0.616$ AU. The mean eccentricity is $< e >= 0.148 \pm 0.086$ and the mean inclination is $< i >= 8.58^{\circ} \pm 6.62^{\circ}$ (Murray & Dermott 2000). However, the exact initial structure of the distribution of asteroids within an asteroid belt immediately after the dispersal of the protoplanetary disk is not fully understood. We assume that the asteroid distribution is sampled from a uniform distribution (Lecar & Franklin 1997). The semi-major axis of each asteroid is given by

$$a_{\rm i} = (a_{\rm max} - a_{\rm min}) \times \chi_r + a_{\rm min}, \tag{3.1}$$

where $a_{\rm min} = 1.558\,{\rm AU}$ is the inner boundary of the distribution, $a_{\rm max} = 4.138\,{\rm AU}$ is the outer boundary, and χ_r is a randomly generated number between 0 and 1. The inner and outer boundaries are determined using the structure of our own solar system, $a_{\rm min}$ is three Hill radii beyond the semi-major axis of Mars and $a_{\rm max}$ is located at three Hill radii interior to Jupiter's orbit. The Hill radius is given by

$$R_{\rm H} = a_{\rm p} \left(\frac{M_{\rm planet}}{3 M_{\rm star}} \right)^{\frac{1}{3}} \tag{3.2}$$

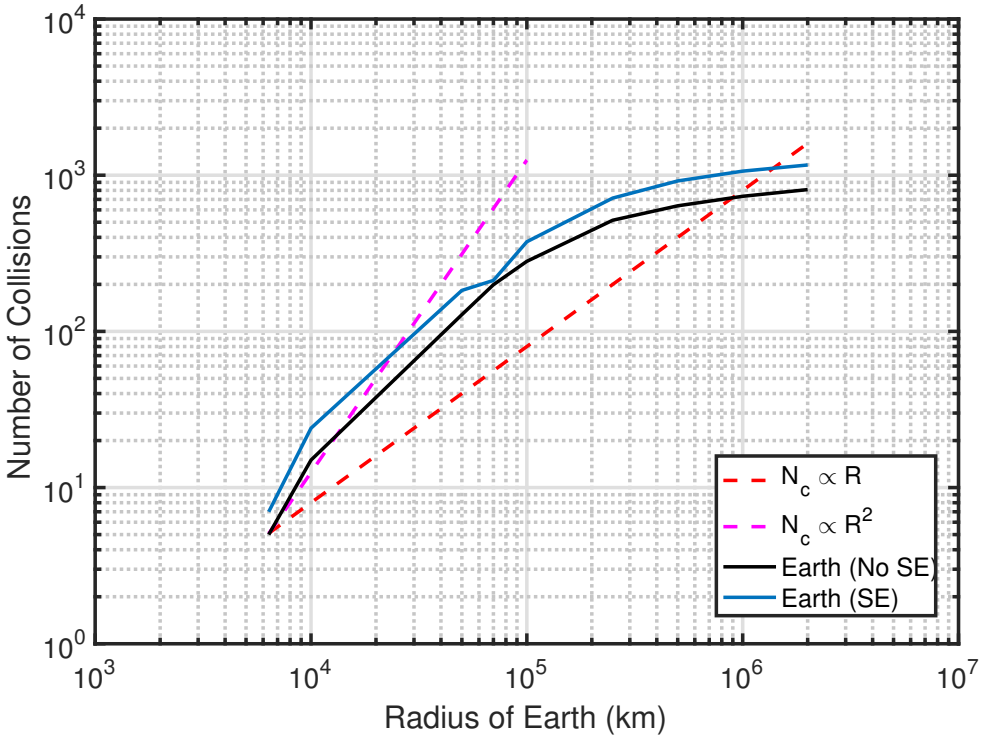

Figure 3.1: A log–log plot showing how the number of asteroid collisions scales with the inflated radius of the Earth, R. The black line shows how the total number of Earth collisions by asteroids (N_c) scales with changing radius of our simulated inflated Earth. The blue lines shows the number of Earth collisions in the presence of a $10\,M_\oplus$ super–Earth at semi–major axis $0.8\,AU$ as a function of inflated Earth radii. The red-dotted line represents the line $N_c(R) \propto R$ and the yellow-dotted line represents the line $N_c(R) \propto R^2$.

where $a_{\rm p}$ is the semi-major axis of the planet and $M_{\rm planet}$ is the mass of the planet. Generally, three Hill radii is the planet's gravitational reach and thus no asteroids would likely be located within this region (Gladman 1993; Chatterjee et al. 2008; Morrison & Malhotra 2015).

First, we checked the scalability of our results with the number of asteroids initially in the belt. We physically inflated the radius of the Earth to be $2 \times 10^6\,{\rm km}$, in order to enhance the number of asteroids on Earth-crossing orbits. We ran a simulation of Earth, Jupiter, Saturn, and a uniformly distributed asteroid belt. The simulation ran for ten million years, with a timestep of eight days with an accuracy parameter of 1×10^{-12}. The accuracy parameter measures approximately how much error per step the variable-timestep symplectic algorithm will tolerate. We ran three simulations

with 10^3, 10^4 and 10^5 asteroids. We found that the number of asteroid collisions scaled linearly with the initial number of asteroids, as we would expect. Thus, to ensure faster simulation times and significant results we took the total number of asteroids in the rest of our work to be 10^4.

Next, in Fig. 3.1, we examined how the number of asteroid collisions with the Earth scales with the radius of the inflated Earth. We ran two series of simulations that included Jupiter, Saturn, the asteroid belt, and the inflated Earth. The first set does not include a Super–Earth while the second set incorporated a super–Earth of mass $10\,M_{\odot}$ at orbital separation $0.8\,AU$. In each series of these simulations we change the radius of the inflated Earth and measure the resulting asteroid collisions with the Earth. If the Earth has a radius of $1\,R_{\oplus}$ then the number of collisions throughout the simulation is only a few. The simulation with the super–Earth always produces a higher rate of collisions than the simulation without a super–Earth and so the effects of the super–Earth occur at all inflated-Earth radii. Thus, inflating the Earth allows for the emergence of trends within the asteroid belt. In order to get statistically significant results we inflated the size of the Earth to $2 \times 10^6\,\mathrm{km}$. Note that since the size of the Earth is inflated, we cannot compare the absolute numbers of asteroid collisions with the Earth with any other outcomes such as collisions with other planets or ejections. We are only able to compare the relative numbers of collisions with an object between simulations.

White Dwarf Pollution

We calculated the evolution of each asteroid orbit for a duration of 50 million years, since this is longer than the cooling age of many white dwarfs. We set up two simulations with a white dwarf mass of $0.5\,\mathrm{M}_{\odot}$ and determined the dynamics of asteroids close to the ν_6 secular resonance and

close to the 2:1 mean-motion resonance, for comparison. Each simulation had a width of $0.5\,\mathrm{AU}$ in initial semi-major axis. The simulation range in semi-major axis for the ν_6 resonance simulation was taken to be $4.2\,\mathrm{AU}$ up to $4.7\,\mathrm{AU}$. The inner boundary of the ν_6 simulation was chosen based on the adiabatic expansion (see equation (5.1)) of the observed inner boundary of the asteroid belt, which is located at $2.1\,\mathrm{AU}$ (Petit et al. 2001). Thus, we only simulated the region that we expect asteroids to be in. The inner and outer boundaries of the 2:1 simulation at $6.31\,\mathrm{AU}$ and $6.81\,\mathrm{AU}$ were chosen to be centered on the location of the resonance at $6.56\,\mathrm{AU}$. The value of $6.56\,\mathrm{AU}$ represents the adiabatic expansion of the average semi-major axis value of the location of the 2:1 mean-motion resonance ($3.27579\,\mathrm{AU}$, Nesvorný & Morbidelli 1998). Note that this simulation had not include any asteroid depletion at the resonance location. Between these boundaries, we placed $20,000$ test particles uniformly within the width of $0.5\,\mathrm{AU}$.

The semi-major axes of Jupiter and Saturn are chosen based on adiabatic expansion (see values for a $0.5\,\mathrm{M}_\odot$ white dwarf in Fig. 5.1). The remaining orbital elements for the planets are taken to be equal to the present-day values, since the solar system is stable over long timescales (Duncan & Lissauer 1998; Ito & Tanikawa 2002).

CHAPTER 4

RESULTS: ASTEROIDAL IMPACTS

We first investigated the influence of the architecture of the inner solar system on the asteroid collisions on Earth. In particular, since Martin & Livio (2015) identified the absence of super–Earths as perhaps the most important architectural element that distinguishes the solar system from other exoplanetary systems, we varied the mass and semi–major axis of an added super–Earth in the inner solar system. The super–Earth's inclination and eccentricity were initially set to zero. To ensure that our simulation with the super–Earth runs correctly, we checked the stability of our system without the asteroid distribution.

Total Number of Earth Collisions

In table 4.1 we show the parameters of twenty-one simulations and the summary of the asteroid collisional outcomes at a time of $10\,\mathrm{Myr}$. We used super–Earth masses in the range $1 - 10\,\mathrm{M}_{\oplus}$ and semi–major axis in the range $0.2 - 1.4\,\mathrm{AU}$. In each simulation we determined the total number of asteroid impacts on the Earth, impacts on the other planets, impacts on the star, the number of asteroids ejected from the system, and the number of asteroids remaining within the distribution. An asteroid is considered to have been ejected if its semi–major axis exceeds $100\,\mathrm{AU}$. Run1 from table 4.1 represents our current solar system as it includes Earth, Jupiter, and Saturn but does not include a super–Earth planet. All of the simulations possessing a super–Earth were compared with

that for our current solar system. Since we have inflated the size of the Earth in order to enhance the number of collisions, we compare only collision rates with the Earth between simulations. We cannot compare the number of collisions with the Earth to the other outcomes of collisions with other bodies or ejections. We include the other outcomes only for completeness.

Table 4.1: Number of asteroidal outcomes for various simulated solar system architectures involving a super–Earth (SE), Earth, Jupiter (J), and Saturn (S). Note that since the size of the Earth has been inflated, the number of Earth impacts cannot be compared to the other outcomes. We only make comparison between the number of Earth impacts between different simulations.

Simulation Name	SE Mass $M_\oplus$	SE Semi-major Axis AU	Earth Impacts	J/S/SE Impacts	Star Collision	Ejected	Remaining
run1	—	—	808	55	2	1112	8023
run2	5	0.22	803	42	1	1135	8019
run3	5	0.40	805	49	1	1121	8024
run4	5	0.50	826	45	3	1138	7988
run5	5	0.60	857	40	4	1115	7984
run6	5	0.70	877	47	1	1131	7944
run7	5	0.80	942	41	1	1121	7895
run8	5	1.20	394	51	1	1169	8385
run9	5	1.40	569	71	2	1221	8138
run10	10	0.22	798	63	1	1125	8013
run11	10	0.40	816	51	1	1122	8010
run12	10	0.50	874	53	3	1106	7964
run13	10	0.60	935	40	2	1118	7905
run14	10	0.70	978	32	2	1143	7845
run15	10	0.80	1236	43	3	1126	7592
run16	10	1.20	310	62	1	1166	8461
run17	10	1.40	615	77	1	1239	8068
run18	1	0.80	801	33	1	1157	8008
run19	2	0.80	843	58	2	1125	7972
run20	3	0.80	868	46	0	1147	7939
run21	4	0.80	913	52	5	1116	7914

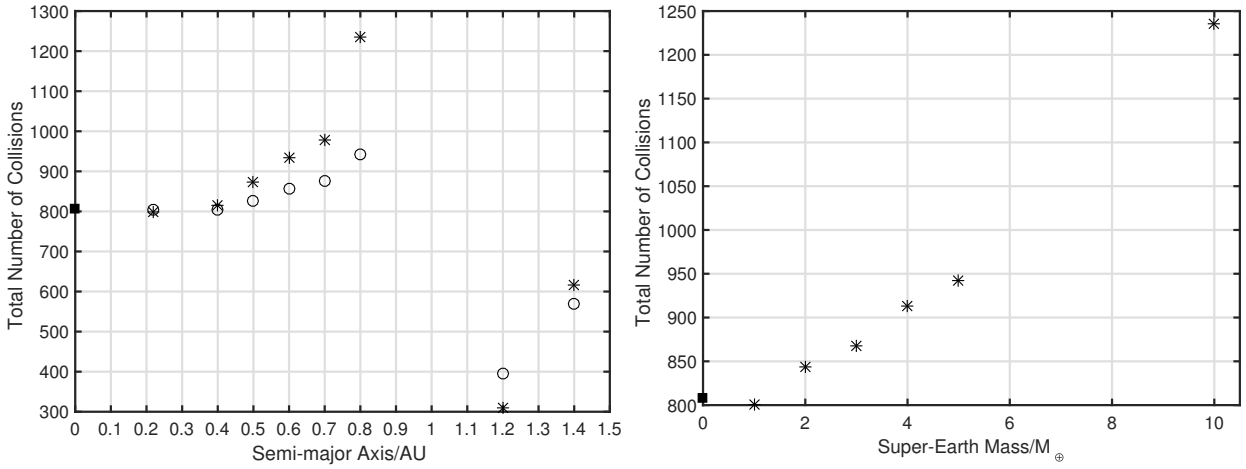

Figure 4.1: *Left Panel:* Total number of asteroid collisions with the Earth as a function of the semi–major axis of the super–Earth. The simulations with a $5M_{\oplus}$ super-Earth are denoted by hollow circles and the simulations with a $10M_{\oplus}$ super-Earth are represented by the star symbols. The square represents the simulation of the standard solar system (without a super-Earth). *Right Panel:* Total number of asteroid collisions with the Earth as a function of super–Earth mass in units of Earth masses ($\mathrm{M}_{\oplus}$) at semi-major axis $a_{\mathrm{SE}} = 0.8\,\mathrm{AU}$.

Fig. 4.1 shows the total number of asteroid collisions with the Earth (left panel) and total number of collisions with the Earth as a function of super–Earth mass with an orbital separation of $0.8\,\mathrm{AU}$ (right panel) after a time of $10\,\mathrm{Myr}$. A super–Earth that is located interior to Earth's orbit increases the asteroid impact rate on the Earth compared to a system without a super–Earth. A super-Earth located exterior to Earth's orbit, decreases the asteroid impact rate compared to a system without a super–Earth. A $10\,\mathrm{M}_{\oplus}$ super-Earth located at a semi-major axis of $0.8\,\mathrm{AU}$ causes the largest number of impacts on Earth, whereas a $10\,\mathrm{M}_{\oplus}$ super-Earth located at a semi-major axis of $1.20\,\mathrm{AU}$ causes the lowest rate of impacts on the Earth. There is a general trend for the total number of asteroid impacts on Earth for super-Earths located interior to Earth's orbit. As the separation of the super-Earth (from the Sun) increases, the asteroid impact flux on Earth also increases.

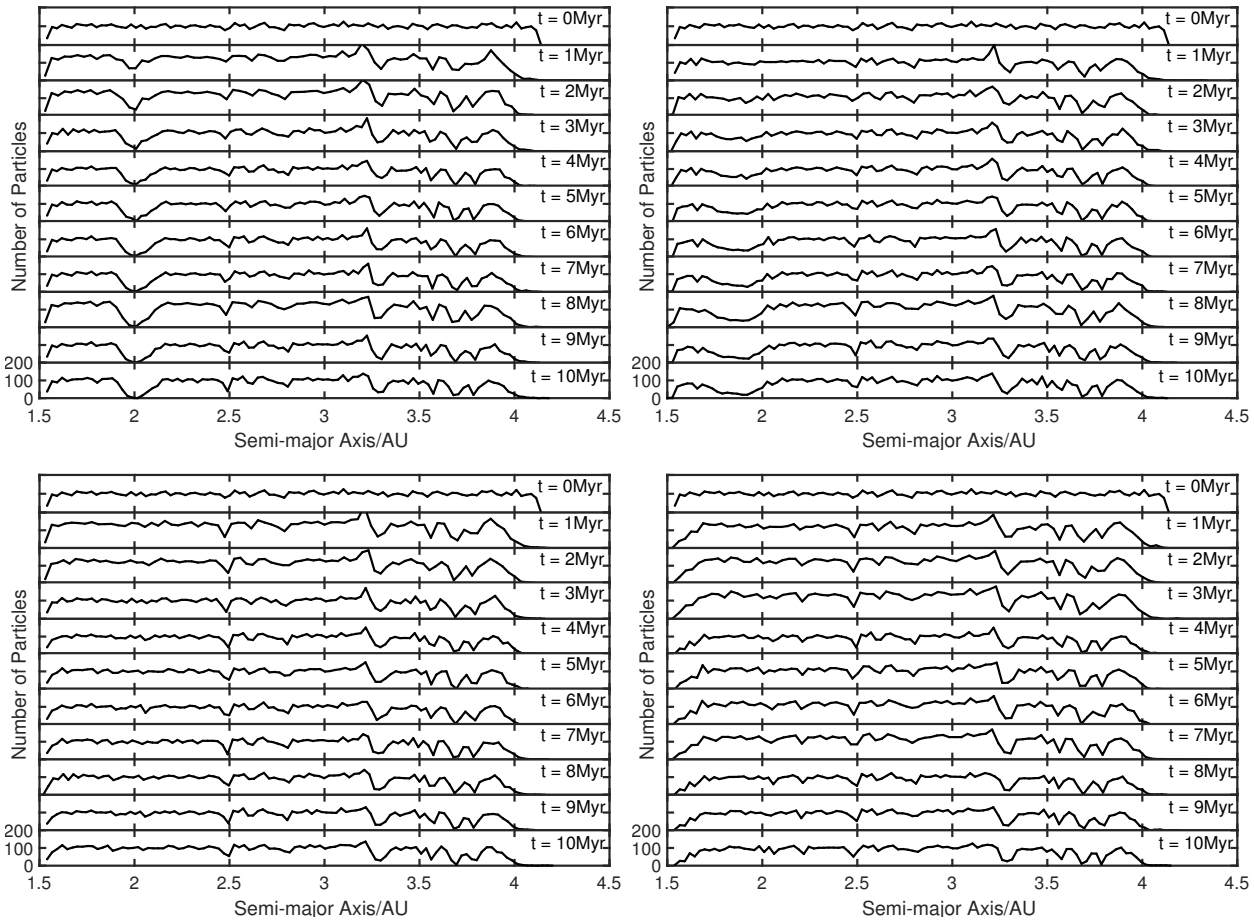

Figure 4.2: Evolution of the asteroid distribution over a span of 10 million years. The asteroid distribution is located in a system containing Earth, Jupiter, Saturn, and a super–Earth (except for the control simulation at top left). The asteroids are initially sampled from a uniform distribution in semi-major axis values, represented at $t = 0\,\mathrm{Myr}$. *Top-Left Panel:* Evolution of asteroid distribution without a super-Earth. *Top-Right Panel:* Evolution of asteroid distribution with a $10M_{\oplus}$ super-Earth located at a semi-major axis of $0.8\,\mathrm{AU}$. *Bottom-Left Panel:* Evolution of asteroid distribution with a $10M_{\oplus}$ super-Earth located at $1.2\,\mathrm{AU}$. *Bottom-Right Panel:* Evolution of asteroid distribution with a $10M_{\oplus}$ super-Earth located at $1.4\,\mathrm{AU}$.

Evolution of the Asteroid Belt

Figure 4.2 shows the evolution of the asteroid belt for simulations involving no super–Earth (top-left panel), a $10\,\mathrm{M}_\oplus$ super–Earth at $a = 0.8\,\mathrm{AU}$ (top-right panel), a $10\,\mathrm{M}_\oplus$ super–Earth at $a = 1.2\,\mathrm{AU}$ (bottom-left panel), and a $10\,\mathrm{M}_\oplus$ super–Earth at $a = 1.4\,\mathrm{AU}$ (bottom-right panel). Each one of these systems also contains Earth, Jupiter, and Saturn. The distribution was calculated every million years for ten million years. As the evolution takes place, areas of the asteroid distribution proceed to be cleared out by gravitational perturbations. These perturbations are the result of mean–motion and secular resonances with Jupiter and Saturn. The most notable mean–motion resonances are the 3:1, 5:2, 7:3, and 2:1, located at $2.5\,\mathrm{AU}$, $2.8\,\mathrm{AU}$, $2.9\,\mathrm{AU}$, and $3.3\,\mathrm{AU}$, respectively. These resonances are located at the same location as our Kirkwood Gaps. Jupiter's chaotic region is located from $3.6\,\mathrm{AU}$ to the outer boundary of the asteroid distribution ($4.133\,\mathrm{AU}$). This region is produced by overlapping libration widths of the mean–motion resonances (Murray & Holman 1997; 1999). The ν_6 resonance is located at $2.0\,\mathrm{AU}$ along with Jupiter's 4:1 mean–motion resonance. The system containing a $10\,\mathrm{M}_\oplus$ super–Earth located at a semi–major axis of $0.8\,\mathrm{AU}$ appears to have a broader ν_6 libration width than a system with no super–Earth. In contrast, if the super–Earth is located exterior to Earth's orbit, the ν_6 resonance completely disappears. We discuss this further in sections 3.3 and 3.5.

Resonances in the Asteroid Belt

There are five potential outcomes for each asteroid during the various simulations. These are: ejection of the asteroid from the solar system, collision with the Earth, collision with another planet, collision with the Sun, or the asteroid remaining in the asteroid belt. Figure 5.3 shows the

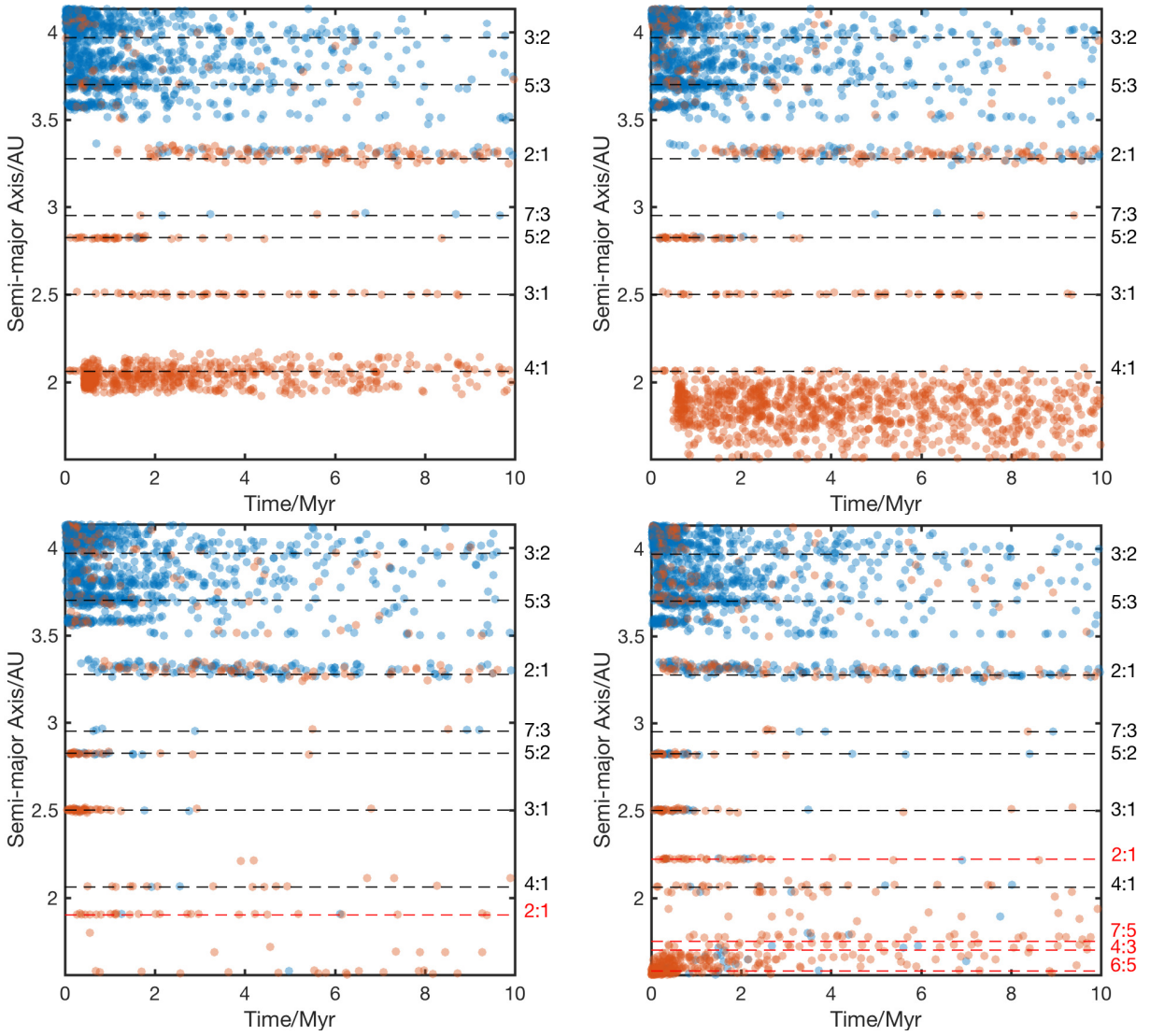

Figure 4.3: The original semi-major axis of each asteroid as a function of the time when the final outcome occurred. The possible outcomes for each asteroid include Earth-impact (red) and other (blue). "Other" refers to ejection, Juptier-impact, Saturn-impact, or colliding with central object. The inner and outer boundary of the asteroid distribution are located at $a_{\rm min} = 1.558\,{\rm AU}$ and $a_{\rm max} = 4.138\,{\rm AU}$. *Top-left Panel:* Asteroid outcomes for a system with no super–Earth. *Top-Right Panel:* $10\,{\rm M}_{\oplus}$ super–Earth located at a semi-major axis of $0.8\,{\rm AU}$. *Bottom-Left Panel:* $10\,{\rm M}_{\oplus}$ super–Earth located at a semi-major axis of $1.2\,{\rm AU}$. *Bottom-Right Panel:* $10\,{\rm M}_{\oplus}$ super–Earth located at a semi-major axis of $1.4\,{\rm AU}$. The mean-motion resonances with Jupiter are represented with the black-dotted line, with the name of each resonance listed to the right of their respected line. The mean-motion resonances with the super–Earth are represented by the red-dotted lines.

various asteroid outcomes for a system with no super–Earth (top–left panel), a $10\,\mathrm{M}_\oplus$ super–Earth located at a semi–major axis $a = 0.8\,\mathrm{AU}$ (top–right panel), a $10\,\mathrm{M}_\oplus$ super–Earth located at $a = 1.2\,\mathrm{AU}$ (bottom–left panel), and a $10\,\mathrm{M}_\oplus$ super–Earth located at $a = 1.4\,\mathrm{AU}$ (bottom–right panel). The initial semi-major axis of each asteroid is shown as a function of the time of its final outcome. The asteroids that were cleared out are originally located at the resonance locations, because mean-motion and secular resonances operate over the initial semi-major axis of each asteroid, increasing the asteroid's eccentricity. On the right hand vertical axis we show the mean–motion resonance locations with Jupiter and the super-Earth. When a $10\,\mathrm{M}_\oplus$ super–Earth is located at $a = 0.8\,\mathrm{AU}$, there is a widening of the ν_6 secular resonance, which increases the number of asteroids perturbed onto Earth-colliding orbits. When the super–Earth is placed exterior to Earth's orbit, there is a substantial decrease in the number of Earth–colliding asteroids. This is due to the ν_6 resonance being suppressed. When the super–Earth is located exterior to Earth's orbit, a 2:1 mean-motion resonance is created within the asteroid belt. This resonance causes additional asteroids to be cleared out. A chaotic zone due to the super–Earth, is seen for the system with a $10M_\oplus$ super–Earth located at $1.4\,\mathrm{AU}$. This chaotic zone is produced from the overlapping libration widths of the super–Earth's 6:5, 4:3, and 7:5 mean-motion resonances. This chaotic zone causes a larger number of asteroids to be cleared out from the inner parts of the asteroid belt.

Collision Rate of the Earth

To determine the frequency of asteroid collisions with the Earth, the asteroid collision rate was calculated and plotted in Fig. 4.4. In the top panel, we show the collision rate for systems with a $10\,\mathrm{M}_\oplus$ super–Earth at various semi-major axis locations and in the bottom panel, the collision

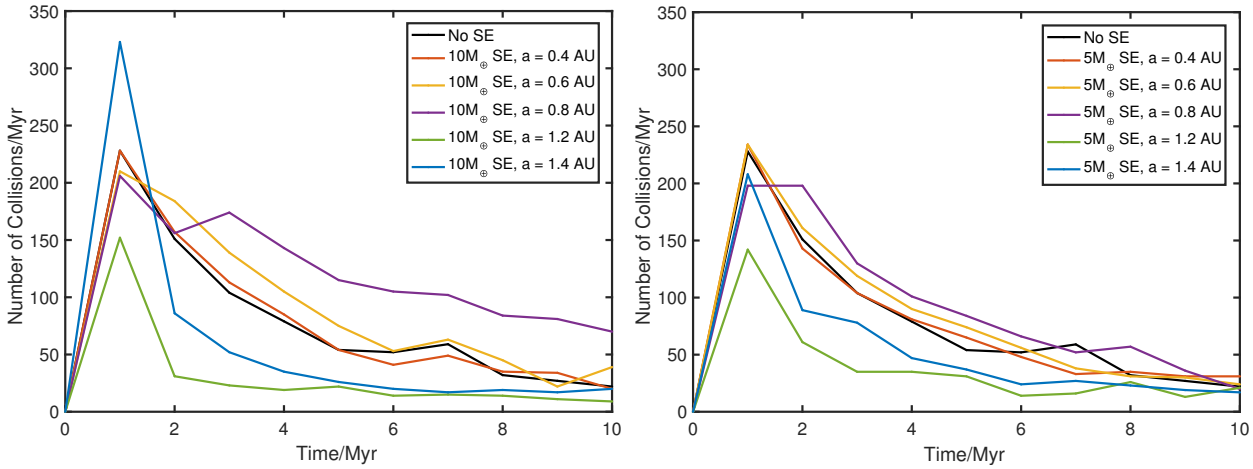

Figure 4.4: Number of asteroid collisions towards Earth per million year for select simulations described in Table 1. *Top Panel:* Collision rate for simulations involving a $10\mathrm{M}_{\oplus}$ super–Earth. *Bottom Panel:* Collision rate for simulations involving a $5\mathrm{M}_{\oplus}$ super–Earth.

rate for systems with a $5\,\mathrm{M}_{\oplus}$ super–Earth for various semi-major axis values. The collision rate was calculated per million years, for ten million years. Initially, the collision rate is higher than compared to later times, due to the fact that there is a larger asteroid population at the beginning of the simulations than at the end. After one million years, the super–Earth located at $1.4\,\mathrm{AU}$ caused the greatest number of collisions, but the rate rapidly declined. This behavior is due to the chaotic region of the super–Earth, which quickly clears out asteroids in locations of overlapping resonances, perturbing them onto Earth–crossing orbits. This chaotic region can be clearly seen in the bottom–right panel in Fig. 5.3. The system with a $10\,\mathrm{M}_{\oplus}$ super–Earth at 0.8AU has the highest asteroid impact rate for the duration of the simulation. When comparing with the simulations that involve $5\,\mathrm{M}_{\oplus}$ super–Earths, the collision rate is also the highest for a super–Earth located at $a = 0.8\,\mathrm{AU}$.

The ν_6 Resonance

The majority of the asteroid collisions with the Earth are from asteroids that originate from the location of the ν_6 resonance in the asteroid belt. Thus, this secular resonance may have played a significant role in making the Earth habitable. In our simulation without a super–Earth, the total number of asteroids that collided with the Earth from secular resonances was about two and a half times that from mean–motion resonances.

The ν_6 secular resonance is due to both Saturn and Jupiter. Jupiter increases the precession frequency of the asteroids so that they fall into a resonance with the apsidal precession rate of Saturn. In Fig. 4.5 we show the precession rate of a test particle as a function of orbital separation. The solid horizontal line denotes the g_6 eigenfrequency of Saturn which is found by calculating the eigenvalues of the matrix A_{ij} associated with a generalized form of the secular perturbation theory (See, e.g., Section 7.7 in Murray & Dermott 2000). The top-left and top-right correspond to the systems which include no super–Earth and a super–Earth located interior to Earth, respectively, and the bottom-left and -right both correspond to systems with a super-Earth located exterior to Earth. The values of Saturn's eigenfrequency for each of these systems are found to be $22.13''\mathrm{yr}^{-1}$, $22.15''\mathrm{yr}^{-1}$, $22.18''\mathrm{yr}^{-1}$, and $22.20''\mathrm{yr}^{-1}$, respectively. The inclusion of a super–Earth has little influence on the value of the g_6 eigenfrequency. We also find that the inclusion of Saturn does not noticeably affect the precession rate of the asteroids–that rate is dominated by Jupiter. The top-left panel of Fig. 4.5 resembles our solar system with the inclusion of Earth, Jupiter, Saturn, and the asteroid belt. The intersection of the particle's precession rate with Saturn's eigenfrequency represents the location of the ν_6 resonance, which is located at $\sim 2\,\mathrm{AU}$.

The inclusion of a super–Earth, which has a mass that is significantly smaller than that of the

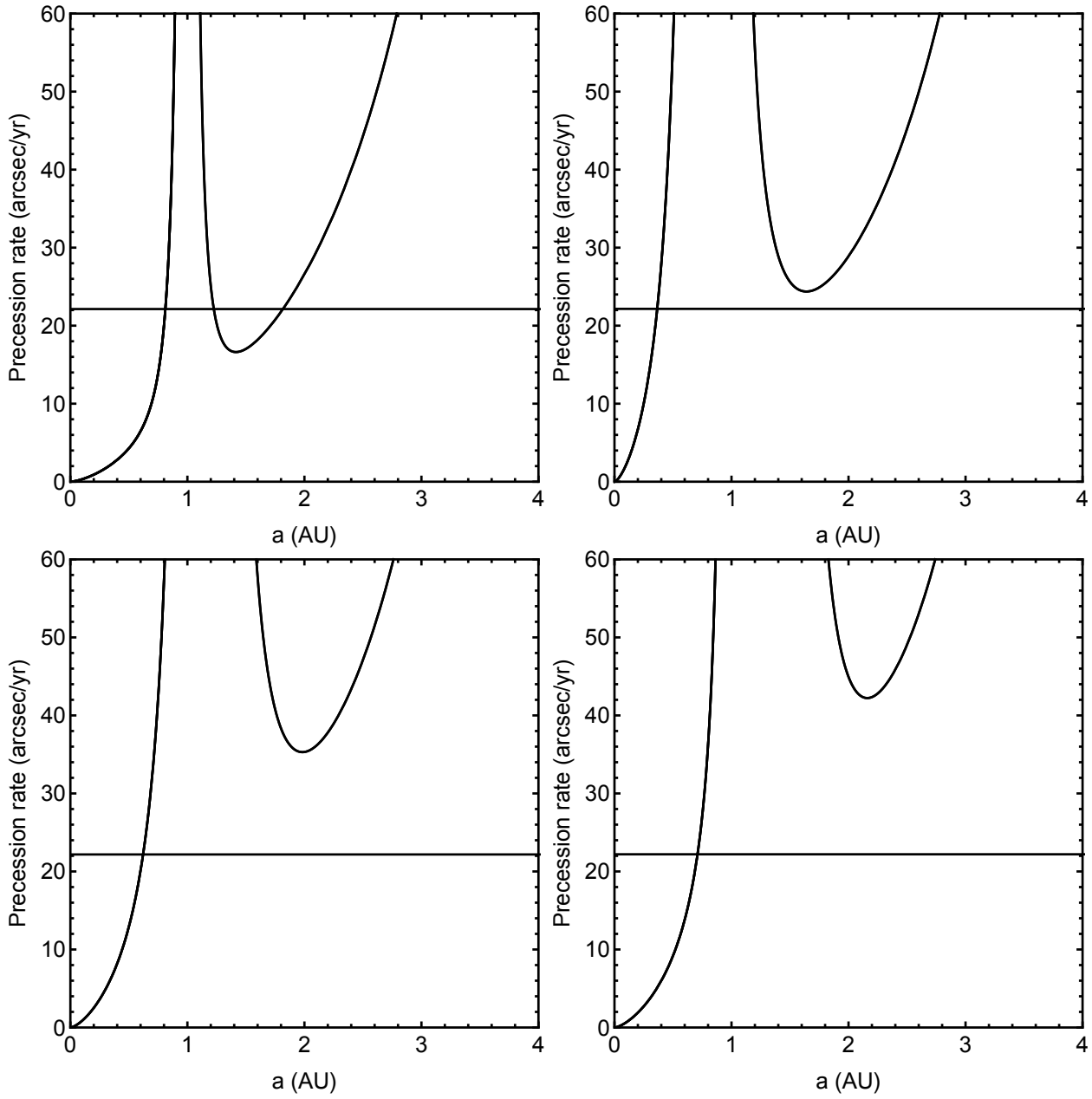

Figure 4.5: The precession rate of a test particle as a function of semi-major axis in the inner part of the solar system. The solid horizontal line represents the g_i eigenfrequency of Saturn. The intersection of the precession rate of the test particle with the eigenfrequency of Saturn denotes the location of a secular resonance. *Top-Left Panel:* A system with no super–Earth. In this case, the intersection located at $2\,\mathrm{AU}$ is the location of the ν_6 resonance within the asteroid belt. *Top-Right Panel:* System with a $10\,\mathrm{M}_\oplus$ super–Earth located at a semi–major axis of $a = 0.8\,\mathrm{AU}$. *Bottom-Left Panel:* System with a $10\,\mathrm{M}_\oplus$ super–Earth located at a semi–major axis of $a = 1.2\,\mathrm{AU}$. *Bottom-Right Panel:* System with a $10\,\mathrm{M}_\oplus$ super–Earth located at a semi–major axis of $a = 1.4\,\mathrm{AU}$.

giant planets Jupiter and Saturn, can lead to a large enough change in the asteroid precession rate to enhance or to remove the resonance with Saturn, depending on the location of the super–Earth. The enhancement of the ν_6 resonance is observed in the top-right panel of Fig. 4.5, where the super–Earth is located interior to Earth's orbit at a semi-major axis $a = 0.80\,\mathrm{AU}$. The precession rate of the test particle is close to the eigenfrequency of Saturn for semi-major axis values from $\sim 1.5\,\mathrm{AU}$ to $\sim 2\,\mathrm{AU}$, which causes an enhancement of the ν_6 resonance.

Re-examining the top-left panel in Fig. 4.5, there are "two" ν_6 resonance locations, located at about $1.3\,\mathrm{AU}$ and $2.0\,\mathrm{AU}$, respectively. When a super–Earth is included within this model at an orbital separation of $0.8\,\mathrm{AU}$, these two resonance locations become closer together as the mass of the super–Earth increases. We follow Malhotra (2012) by constructing a analytical toy model of the ν_6 resonance width by calculating the forced maximum eccentricity of a test particle near the ν_6 resonance with and without a super–Earth. When the mass of the super–Earth reaches $10\,\mathrm{M}_\oplus$, the widths of the two ν_6 resonances converge, forcing the resonance to operates over a larger range of semi-major axis values, this in turn, causes an enhancement of the resonance.

The removal of the ν_6 resonance occurs when the super–Earth is located exterior to Earth's orbit. This can be seen in the bottom-left panel (super–Earth located at $a = 1.2\,\mathrm{AU}$) and the bottom-right panel (super–Earth located at $a = 1.5\,\mathrm{AU}$) of Fig. 4.5, where the precession rate of the test particle does not intersect with the eigenfrequency of Saturn, leading to the disappearance of the ν_6 resonance. This analysis of the precession rate of a test particle agrees with the results described in the previous Section. Re-examining Fig. 5.3, we can see that when the super–Earth is located interior to Earth's orbit we have a widening of the libration width ($\sim 1.5\,\mathrm{AU}$ to $\sim 2.0\,\mathrm{AU}$) of the ν_6 resonance, whereas if the super–Earth is located exterior to Earth's orbit, the resonance is removed. Thus, the enhancement or removal of the ν_6 resonance is predicated on the location of

the super–Earth.

We next considered the properties of the outer giant planets that produce a ν_6 resonance in the location of the asteroid belt. We keep the mass and orbital separation of Jupiter fixed. The location of the ν_6 resonance as a function of Saturn's semi-major axis and mass is shown in Fig. 4.6. In the left panel, the location of the ν_6 resonance as a function of Saturn's semi-major axis was found by calculating the resulting eigenfrequency of Saturn and then finding the location of the intersection with the precession rate of a test particle. The precession frequency of the test particle was calculated by including the planets Earth, Jupiter, and Saturn. However, Saturn's eigenfrequency was calculated by including only Jupiter since the Earth has a negligible influence in the calculation. We included a correction due to the near 2:1 mean-motion resonance between Jupiter and Saturn (Malhotra et al. 1989; Minton & Malhotra 2011). The location of the resonance drastically moves outwards as Saturn becomes closer to a 2:1 resonance with Jupiter at about $8.3\,\mathrm{AU}$. As Saturn moves outwards, the resonance location moves inwards. The right panel of Fig. 4.6 shows the location of the ν_6 resonance as a function of Saturn's mass, while Saturn is located at its current semi-major axis of $9.5\,\mathrm{AU}$. We direct the readers to a more accurate calculation of Minton & Malhotra (2011)(see their figure 2) for the value of g_6 and the ν_6 location as a function of Saturn's semi-major axis. If we increase Saturn's mass, then the location of the resonance moves outwards slightly. For a mass that is one tenth of its current value, the resonance moves inwards only slightly. The resonance location is rather more sensitive to the orbital separation than to the mass of Saturn.

We have run additional numerical simulations of the asteroid belt to consider the effects of varying the properties of the outer giant planets. We varied Saturn's semi-major axis and mass to verify the trends found in Fig. 4.6. The results of these simulations are presented in Table 4.2. Varying Saturn's semi–major axis (runs 22-27 from Table 4.2) follows the trend calculated in

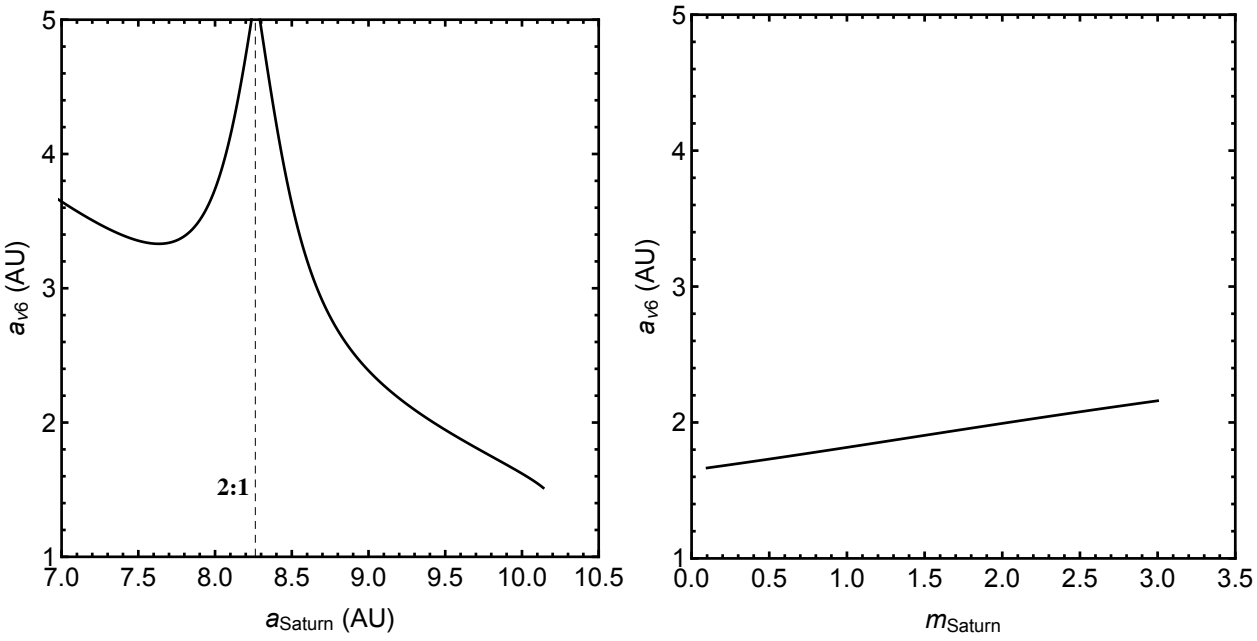

Figure 4.6: *Left Panel:* Location of the ν_6 secular resonance with respect to the semi-major axis of Saturn. A correction was implemented due to the near 2:1 mean-motion resonance between Jupiter and Saturn (Malhotra et al. 1989; Minton & Malhotra 2011). The dotted line shows the location of this 2:1 mean-motion resonance. *Right Panel:* Location of the ν_6 resonance as a function of the mass of Saturn.

Fig. 4.6 (left panel). As Saturn's semi-major axis increases, the location of the ν_6 resonance moves outside the asteroid belt boundaries. On the other hand, when the semi–major axis decreases, the ν_6 resonance moves towards the middle/outer regions of the asteroid belt. This change in the location of the resonance can be seen in Fig. 4.7, where the left panel represents the various asteroid outcomes when Saturn is located at a semi–major axis of $a = 8.0\,\mathrm{AU}$ and the right panel shows the outcomes for when Saturn is located at $a = 12.0\,\mathrm{AU}$. Again, the time of the particular outcome is plotted with respect to the initial semi-major axis of each asteroid.

For the case where Saturn is located at $a = 8.0$, the location of the ν_6 resonance is shifted outward to approximately $3.5\,\mathrm{AU}$, which is what is expected according to the left panel of Fig. 4.6. This movement of the resonance causes a decrease in the number of collisions with the Earth, but

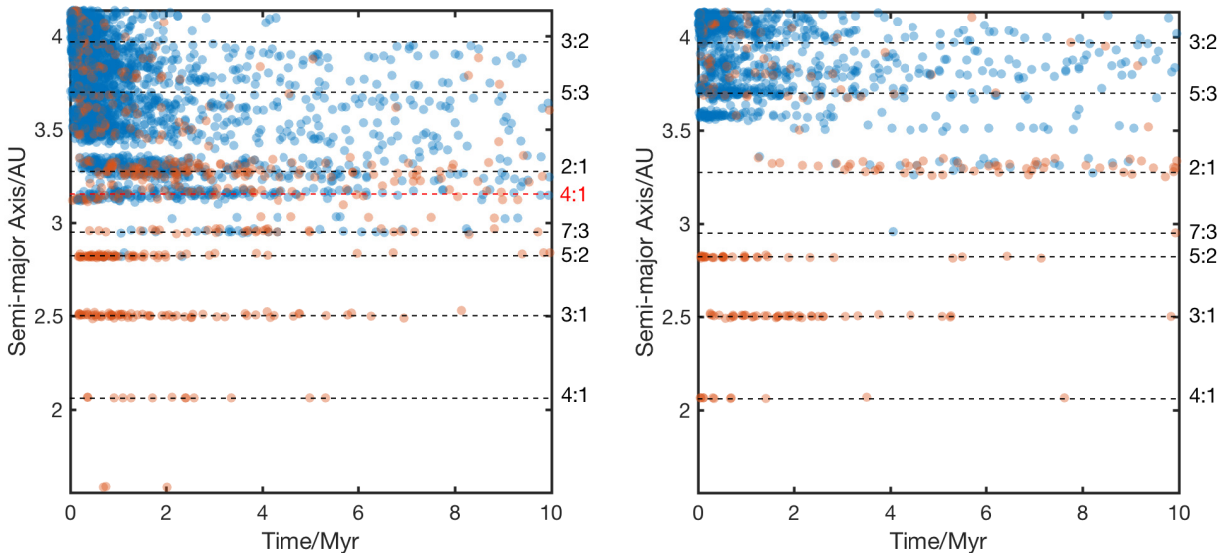

Figure 4.7: The original semi-major axis of each asteroid as a function of the time when the final outcome occurred. The possible outcomes for each asteroid include Earth-impact (red) and other (blue). "Other" refers to ejection, Juptier-impact, Saturn-impact, or colliding with central object. The inner and outer boundary of the asteroid distribution are located at $a_{min} = 1.558\,\mathrm{AU}$ and $a_{max} = 4.138\,\mathrm{AU}$. *Left Panel:* Asteroid outcomes for a system with Saturn located at a semi-major axis $a = 8\,\mathrm{AU}$. *Right Panel:* Saturn located at a semi–major axis $a = 12\,\mathrm{AU}$. The mean–motion resonances with Jupiter are represented with the black–dotted line and the red-dotted line represents a mean-motion resonance between the asteroids and Saturn. Each mean-motion resonance is listed to the right of their respected line.

causes a significant increase in the number of asteroid ejections. For the situation where Saturn's semi-major axis is taken to be $12.0\,\mathrm{AU}$, there is no ν_6 secular resonance. The disappearance of the resonance is caused by there being no intersection of the particles precession rate with Saturn's eigenfrequency. Overall we find that varying the orbital separation of Saturn in both directions has a significant effect on the location of the ν_6 secular resonance and that it generally leads to a decrease in the number of asteroid collisions. However, the orbital location of Saturn may not be accidental, since it is close to being in the 5:2 resonance with Jupiter. Fernandez & Ip (1984); Fernández & Ip (1996) suggested the jovian planets proximity to the current near resonant structure could be a consequence of the differential expansion of their orbits during late stages of planetary formation (e.g. Michtchenko & Ferraz-Mello 2001).

When the mass of Saturn is changed (runs 28-31 from Table 4.2), the calculated trend in Fig. 4.6 (right panel) breaks down for masses greater than $1.5\,\mathrm{M_{Saturn}}$ (results not shown in Table 4.2). For the situations where Saturn's mass is greater than $1.5\,\mathrm{M_{Saturn}}$, the Earth's orbit becomes highly eccentric ($e \approx 0.5$) which causes a higher number of asteroid impacts. When Saturn has a mass of $0.1\,\mathrm{M_{Saturn}}$ the number of asteroid collisions with Earth is substantially lower, since the ν_6 resonance is located outside the asteroid distribution. The location of the ν_6 resonance is more sensitive to changes in Saturn's orbital separation than to its mass.

Table 4.2: Number of asteroidal outcomes with varying parameters of Saturn. Each simulation includes Earth, Jupiter (J), and Saturn (S). Note that since the size of the Earth has been inflated, the number of Earth impacts cannot be compared to the other outcomes. We only make comparison between the number of Earth impacts between different simulations .

Simulation Name	Saturn Mass M_S	Saturn Semi-major Axis AU	Earth Impacts	J/S Impacts	Star Collision	Ejected	Remaining
run22	1.0	8.0	514	113	2	2705	6666
run23	1.0	9.0	1012	37	0	1206	7745
run24	1.0	9.537	808	55	2	1112	8023
run25	1.0	10.0	957	48	4	1034	7957
run26	1.0	11.0	248	50	1	966	8735
run27	1.0	12.0	210	54	1	928	8807
run28	0.1	9.537	172	83	1	874	8870
run29	0.5	9.537	447	55	2	1005	8491
run30	1.0	9.537	808	55	2	1112	8023
run31	1.5	9.537	1163	49	3	1238	7547

CHAPTER 5

RESULTS: WHITE DWARF POLLUTION

Solar System

In this Section we first consider how our solar system evolves once our Sun becomes a white dwarf. We assume that the terrestrial planets, up to the Earth, become engulfed in the Sun (Schröder & Connon Smith 2008), while the orbits of the giant planets and the asteroid belt expand adiabatically. We model the evolution of the ν_6 resonance in the solar system first analytically and then numerically with N–body simulations of the asteroid belt with the remaining planetary system.

Analytic Results

Here we examine the resonance location and the resonance width for the ν_6 resonance in the solar system both before and after the Sun becomes a white dwarf. The ν_6 secular resonance properties are affected by both Saturn and Jupiter (Bottke et al. 2000; Ito & Malhotra 2006). Jupiter increases the precession frequency of the asteroids so that they fall into a resonance with the apsidal precession rate of Saturn. The location of the ν_6 resonance is found by calculating the location of intersection of a test particle's precession rate with Saturn's eigenfrequency.

The semi-major axes of the planets are assumed to undergo adiabatic expansion based on the

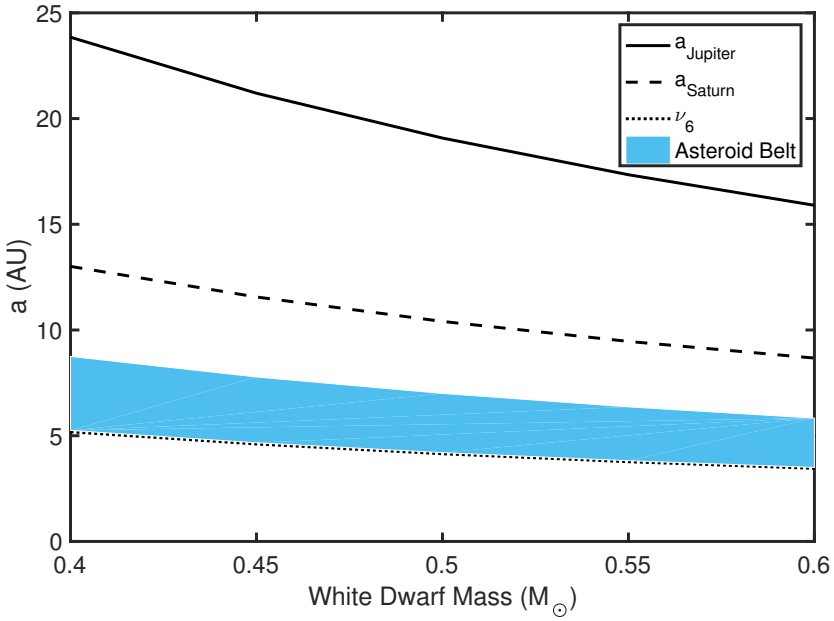

Figure 5.1: The semi-major axes of Saturn, Jupiter, and the ν_6 secular resonance as a function of white dwarf mass. The location of the ν_6 resonance was found by calculating the location of intersection of the asteroids precession rate with the eigenfrequency of Saturn. Both Jupiter and Saturn's orbital separation depend on the adiabatic expansion which is proportional to the ratio of the initial stellar mass to the white dwarf mass (see equation 5.1). The location of the adiabatically expanded asteroid belt as a function white dwarf mass is shown by the red-shaded region.

ratio of the initial stellar mass to the white dwarf mass,

$$a_{\rm final} = a_{\rm initial} \left(\frac{m_*}{m_{\rm wd}} \right) . \tag{5.1}$$

Fig. 5.1 shows the location of Jupiter, Saturn, and the ν_6 secular resonance with Saturn as a function of white dwarf mass. We consider white dwarf masses in the range $0.4\,{\rm M}_\odot$ to $0.6\,{\rm M}_\odot$ as expected for the Sun (Liebert et al. 2005; Falcon et al. 2010; Tremblay et al. 2016). For our standard model we choose a mass of $0.5\,{\rm M}_\odot$ (e.g. Sackmann et al. 1993; Schröder & Connon Smith 2008). The location of the adiabatically expanded asteroid belt as a function of white dwarf mass is shown by the blue-shaded region. We use the observed inner and outer boundaries of the asteroid belt to

produce this region. The observed inner boundary of our asteroid belt is currently at $2.1\,\mathrm{AU}$. We find that this value is consistent with our analytical models where the intersection of the particle's precession rate with Saturn's eigenfrequency is located at about $2\,\mathrm{AU}$. The outer boundary of the asteroid belt is currently located at about $3.5\mathrm{AU}$ due to Jupiter's chaotic region.

Figure 5.2 demonstrates the width of the ν_6 resonance during the main-sequence stage of stellar evolution (solid line) versus the post-main-sequence stage (dotted line). The main sequence stage includes Earth, Jupiter and Saturn at semi-major axes $1.0\,\mathrm{AU}$, $5.2\,\mathrm{AU}$, and $9.5\,\mathrm{AU}$, respectively. The post-main-sequence stage only includes Jupiter and Saturn with orbital separations of $10.4\,\mathrm{AU}$ and $19.0\,\mathrm{AU}$, respectively, assuming that the Earth would be engulfed during the RGB phase of stellar evolution. The x-axis is normalized with respect to the semi-major axis of Jupiter in order to show the comparison. The resonance has shifted outwards into a region of the asteroid belt that would have previously contained stable asteroids. These asteroids are unstable to resonant perturbations and may be a source of pollution for white dwarfs.

Unlike the mean–motion resonances, the width of the ν_6 secular resonance does not vary with the mass of the white dwarf. The observed difference in Fig. 5.2 is due to the engulfment of the Earth during the post-main-sequence stages. This changes the calculated eigenvectors ($E_j^{(6)}$) which corresponds to the resonance being shifted outward. This result is somewhat surprising and means that this model of white dwarf pollution requires a terrestrial planet to be engulfed in order to change the resonance.

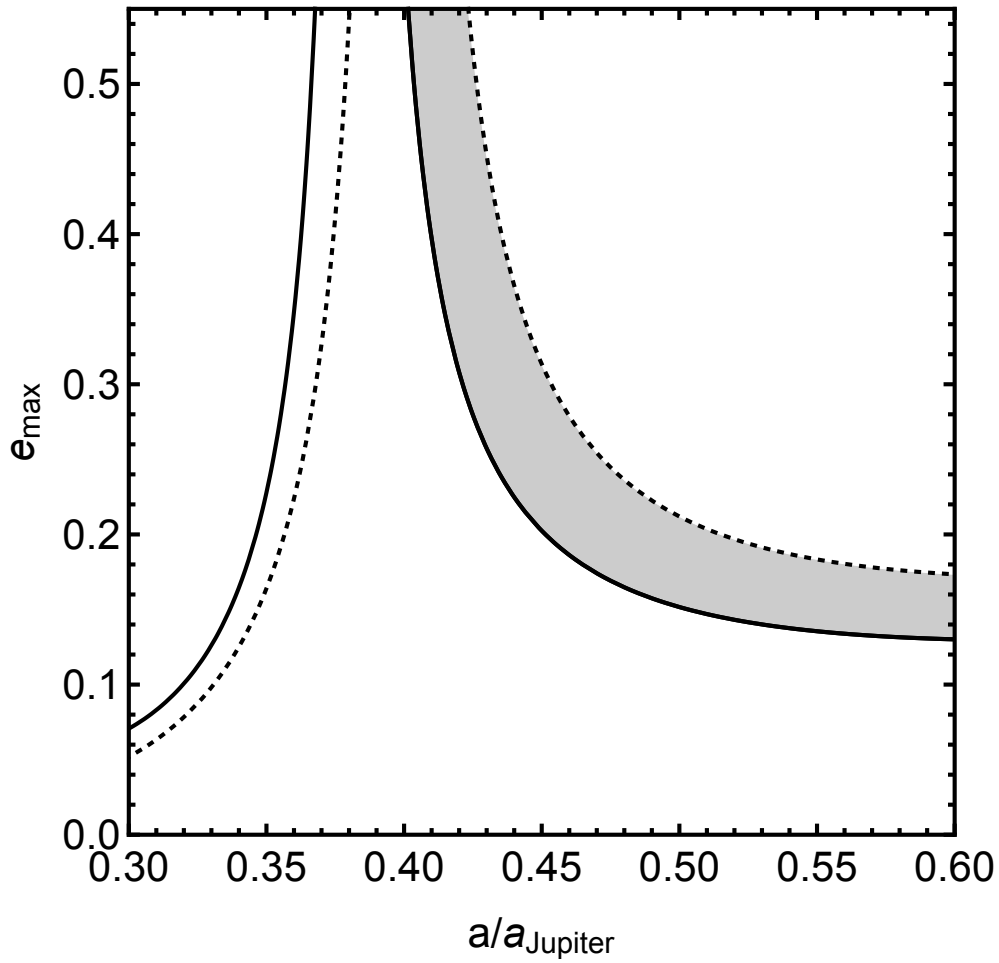

Figure 5.2: The width of the ν_6 secular resonance during main-sequence stage (solid-black lines) versus post-main-sequence stage (dotted-black lines). The width during main-sequence was calculated with the planets, Earth, Jupiter, and Saturn. As the star evolves during the post-main-sequence stage, we assume the Earth is engulfed. The stellar mass loss shifts the ν_6 resonance outwards due to this engulfment, allowing previously stable asteroids to undergo secular perturbations. The shaded region represents the region of previously stable asteroids that undergo increased eccentricity growth due to secular resonant perturbations.

Numerical Results

We tested the analytic models of the previous section with N-body simulations of an asteroid belt around a white dwarf. We used the hybrid symplectic integrator in the orbital dynamics package, MERCURY, to model the structure of the asteroid belt and the tidal disruption rate around a $0.5\,\mathrm{M}_\odot$ white dwarf. MERCURY uses N-body integrations to calculate the orbital evolution of objects moving in the gravitational field of a large body (Chambers 1999). We simulated the motion of Jupiter, Saturn, and a distribution of asteroids orbiting a white dwarf star. The asteroids in our simulations were point particles that do not interact gravitationally with one another but do interact gravitationally with the planets and the white dwarf. We may neglect the asteroid-asteroid interactions because the timescale for such collisional interaction is much longer than the timescale for the action of perturbations by resonance effects. The timescale for resonant effects is of the order of $\sim 1\,\mathrm{Myr}$ (Ito & Tanikawa 1999), whereas some of the largest asteroids have collisional timescales that are of the order of the age of the solar system (Dohnanyi 1969).

As the asteroids are scattered from the asteroid belt due to secular resonances, the asteroids become tidally disrupted by the white dwarf if they pass within a tidal disruption radius given by

$$\begin{aligned} R_{\rm tide} &= C_{\rm tide} R_{\rm wd} \left(\frac{\rho_{\rm wd}}{\rho_{\rm ast}} \right)^{1/3} \\ &\approx 1.3 \left(\frac{C_{\rm tide}}{2} \right) \left(\frac{M_{\rm wd}}{0.6 M_\odot} \right)^{1/3} \left(\frac{\rho_{\rm ast}}{3 \mathrm{g\,cm^{-3}}} \right)^{-1/3} R_\odot, \end{aligned} \tag{5.2}$$

(Davidsson 1999; Jura 2003; Bear & Soker 2013), where $M_{\rm wd}$, $R_{\rm wd}$, $\rho_{\rm wd}$ are the mass, radius, and density of the white dwarf, respectively, and $\rho_{\rm ast}$ is the density of the asteroid. $C_{\rm tide}$ is a numerical constant that depends on the orbital parameters of the asteroid, its rotation, and composition (Davidsson 1999; Jura 2003). We took $C_{\rm tide} = 2$ for a solid non-synchronized asteroid (Bear &

Soker 2013). Since the asteroids in our simulations are non self-interacting point-particles, we assumed the average density of the asteroids to be $3\,\mathrm{g\ cm^{-3}}$ (Krasinsky et al. 2002) in order to calculate the tidal disruption radius for the $0.5\,\mathrm{M_\odot}$ WD to be $R_{\mathrm{tide}} = 1.22\,\mathrm{R_\odot}$. Within our simulations, we physically inflated the size of the white dwarf to have a radius equal to the tidal disruption radius. When an asteroid passes within the tidal disruption radius it is considered tidally disrupted and then removed from the simulation.

The numerical simulations aimed to determine the number of tidally disrupted asteroids from two different locations in the asteroid belt, the ν_6 secular resonance and the 2:1 mean-motion resonance. Figure 5.3 summarizes the results of these numerical simulations. The ν_6 simulation is shown in the left panel and the 2:1 mean-motion simulation is given by the right panel. The outcomes for each asteroid include ejection (blue dots) and tidal disruption (red dots). Since mean-motion resonances move linearly during adiabatic expansion, the majority of the asteroids located within the 2:1 resonance would have been depleted by the time the star evolved to become a white dwarf. In our simulation, we have not taken account of any depletion and therefore the number of tidal disruption events is highly over estimated. However, the number of asteroids tidally disrupted is still significantly higher for the ν_6 resonance than for the 2:1 resonance, even though the number of tidal disruption events for the 2:1 resonance is really an upper limit. The ratio of the number of ejections to tidal disruptions is higher for the 2:1 mean-motion resonance than for the ν_6 resonance. This suggests that the 2:1 mean-motion resonance is not nearly as efficient in producing tidal disruption events as is the ν_6 secular resonance.

Finally, we calculated the tidal disruption rate for the ν_6 resonance case. This is an important aspect of white dwarf pollution because for this mechanism to be a major contributor there needs to be a continuous supply of asteroids. Figure 5.4 shows the normalized number of tidally disrupted

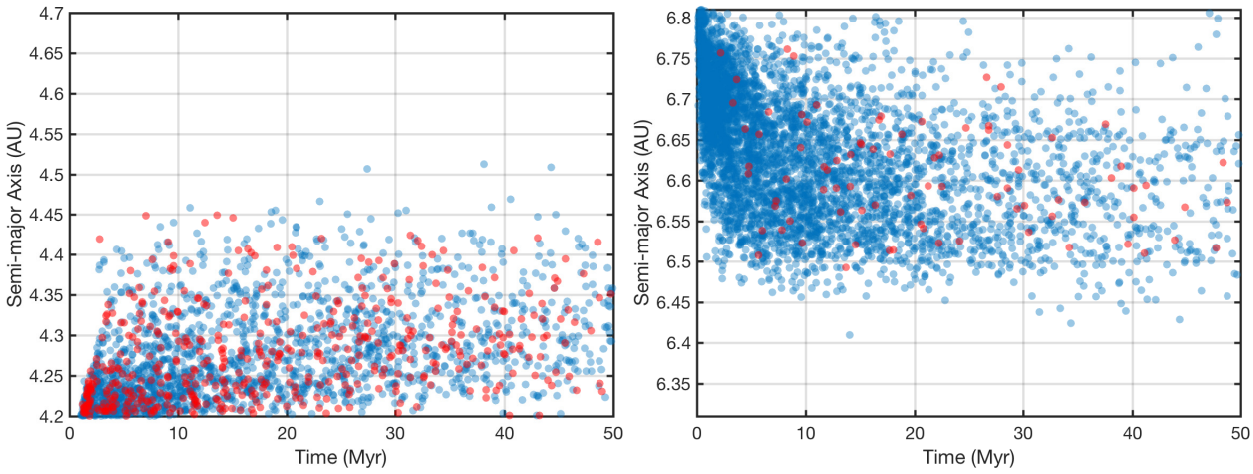

Figure 5.3: N-body simulations of the evolution of asteroids near the ν_6 secular resonance (left panel) and near the 2:1 mean-motion resonance (right panel) around a $0.5\,\mathrm{M}_{\odot}$ white dwarf. The outcomes for each asteroid include ejection (blue dots) and tidal disruption (red dots). Each simulation is comprised of 20,000 test particles initially distributed uniformly over a width of 0.5 AU. Because mean-motion resonances move linearly during adiabatic expansion, the majority of asteroids located within the 2:1 resonance would have been depleted by the time the star evolved to become a white dwarf. In our simulation, we assume there is no depletion in order to compare the number of tidal disruption events to the ν_6 secular resonance. The inner boundary of the ν_6 simulations were produced by knowing that the observed inner boundary of our asteroid belt is located at $2.1\,\mathrm{AU}$. Thus, all of the tidal disruption events during the ν_6 simulations occur on previously stable asteroids that have survived the process of stellar evolution.

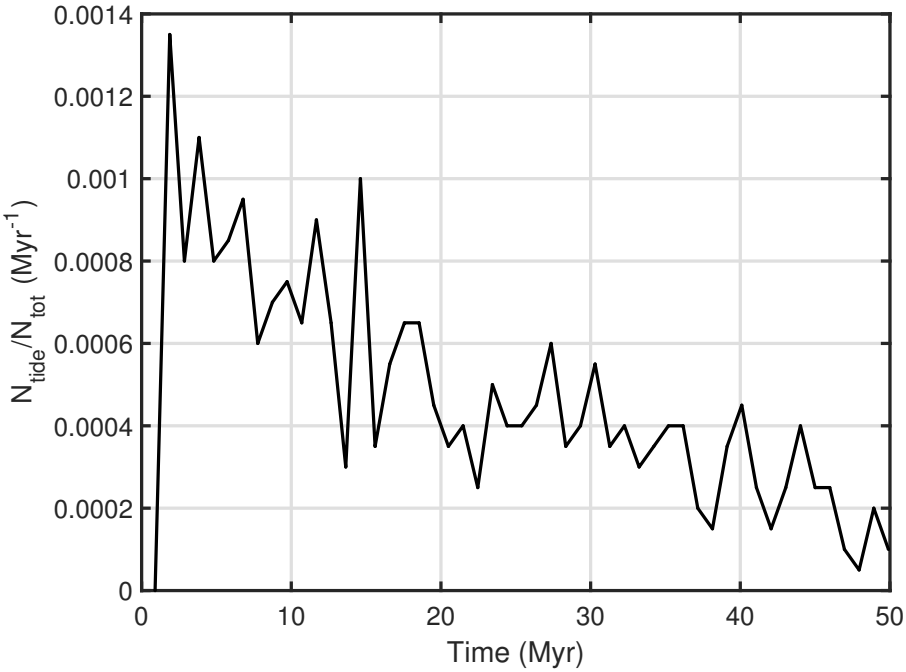

Figure 5.4: The number of tidally disrupted asteroids as a function of time for the ν_6 secular resonance simulation from Fig. 5.3 for a $0.5\,\mathrm{M}_\odot$ white dwarf. The number of tidal disruption events is normalized to the initial number of test particles in our simulations. The rate shows a slowly decreasing continuous stream of tidally disrupted asteroids.

asteroids as a function of time for the evolution of asteroids near the ν_6 secular resonance. There is a continuous rate of tidal disruptions throughout the simulation. White dwarf pollution is observed at $30\,\mathrm{Myr}$ to $600\,\mathrm{Myr}$ cooling ages, thus our simulation time of 50 million years is longer than the observed lower limit of pollution cooling age. Our results therefore contain encouraging evidence for white dwarf pollution through secular resonant mechanisms.

Koester et al. (2014) conducted an unbiased survey for DA white dwarf metal pollution with cooling ages in the range of $20 - 200\,\mathrm{Myr}$ and temperature $17,000\mathrm{K} < \mathrm{T_{eff}} < 27,000\mathrm{K}$. Using previous ground-based studies and adopting bulk Earth abundances for the debris disks, mass accretion rates range from a few $10^5\,\mathrm{g\,s^{-1}}$ to a few $10^8\,\mathrm{g\,s^{-1}}$. Their conclusions suggest that at least 27% of all white dwarfs with cooling ages $20 - 200\,\mathrm{Myr}$ are accreting planetary debris, but that

fraction could be as high as about 50%. Since the diffusion timescale is of the order of days to weeks for polluted DA white dwarfs, an assumption of steady state between accretion and diffusion can be assumed. Steady state means a constant diffusion flow of each element throughout the atmosphere, which equals the accretion flow (Koester et al. 2014)

$$X\rho v_{\rm diff} = \text{const.} = X_{\rm acc}\dot{m}_{\rm acc}, \tag{5.3}$$

where X is the mass fraction of the specified element, ρ is the mass density in the atmosphere, and $v_{\rm diff}$ is the diffusion velocity. $X_{\rm acc}$ is the abundance in the accreted matter and $\dot{m}_{\rm acc}$ is the accretion rate per unit area. For a large fraction of polluted white dwarfs in the optical, only Ca II is detected as the elemental pollutant. Consequently, accretion rate calculations are typically derived using the infall rate for calcium, giving the mass accretion rate as

$$\dot{M}_z \approx \frac{1}{A}\frac{X_{\rm Ca}M_{\rm CVZ}}{\tau_{\rm Ca}}, \tag{5.4}$$

(Farihi 2016) where A is the mass fraction of calcium within the accreted material, $X_{\rm Ca}$ is the mass fraction of calcium, $M_{\rm CVZ}$ is taken as the mass of the outer stellar convective layers where any heavy elements are well-mixed, and $\tau_{\rm Ca}$ is the exponential diffusion timescale for calcium.

We estimate the mass accretion rate for our secular resonance model based on the tidal disruption rate of $0.0002\,{\rm Myr}^{-1}$ calculated from Fig. 5.4. Multiplying this rate by the mass of the asteroid belt ($M_{\rm belt} = 3.6 \times 10^{24}\,{\rm g}$; Krasinsky et al. 2002) we obtain a mass accretion rate of order $10^7\,{\rm g\,s}^{-1}$ which is in good agreement with observations, see Fig. 10 in Farihi (2016).

The results of our N–body simulations agree with the analytic model presented previously. The

left panel of Figure 5.3 shows that the location of the ν_6 resonance has shifted outwards into the asteroid belt as predicted analytically in Figure 5.2. In the next Section we consider how secular perturbations may apply more generally to exoplanetary systems with the analytic model of the secular resonance.

Exoplanetary Systems

Secular resonances are sensitive to the architecture of a planetary system (e.g Minton & Malhotra 2011; Smallwood et al. 2017). In this Section we consider how the ν_6 secular resonance may pollute a white dwarf for different planetary architectures with the analytic model described in Chapter 2. First, we look at the dynamics of the ν_6 secular resonance location for varying mass and location of Saturn in the Solar System. Next, we examine the location of secular resonances in planetary systems with a binary star companion.

Here we examine a system with two outer giant planetary companions around a white dwarf. In order to generalize our results to exoplanetary systems, we calculated how the resonance location changes with the semi-major axis and mass of the outer planetary companion. We model three architectures with the inner planetary companion a Jupiter-mass planet with semi-major axes $6\,\mathrm{AU}$, $10.4\,\mathrm{AU}$, and $30\,\mathrm{AU}$. The value of $30\,\mathrm{AU}$ was based on a theoretical adiabatic expansion of the planet $\mathrm{HR}\,8799\mathrm{e}$. The system $\mathrm{HR}\,8799$ houses a warm planetesimal belt (Moro-Martín et al. 2010) interior to $\mathrm{HR}\,8799\mathrm{e}$, which has a semi-major axis of $15\,\mathrm{AU}$ (Marois et al. 2010) around a $1.56\,\mathrm{M}_{\odot}$ type A star (Baines et al. 2012; Goździewski & Migaszewski 2014).

The location of the secular resonance as a function the outer companion's semi-major axis is found by calculating the resulting eigenfrequency of the outer companion and then finding the

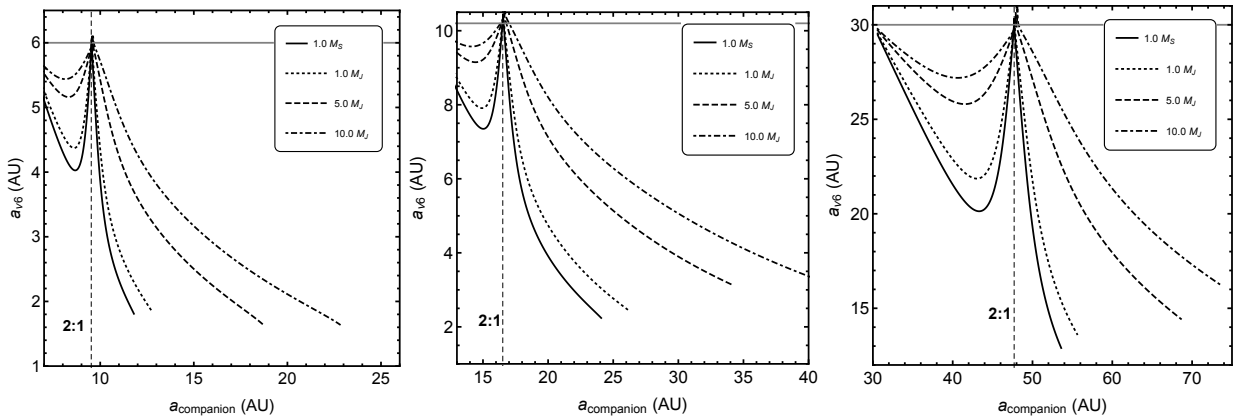

Figure 5.5: Location of the ν_6 secular resonance with respect to the semi-major axis of various planetary companions for white dwarf mass $M_{\rm wd} = 0.5\,{\rm M}_\odot$. The semi-major axis of the inner companion is constant at $6\,{\rm AU}$ (left panel), $10.4\,{\rm AU}$ (middle panel), and $30\,{\rm AU}$ (right panel). The masses of the outer planetary companions that are considered include 1.0 Saturn mass ($M_{\rm s}$, solid), 1.0 Jupiter mass ($M_{\rm J}$, dotted), $5.0\,M_{\rm J}$ (dashed), and $10.0\,M_{\rm J}$. A correction was implemented due to the near 2:1 mean-motion resonance between Jupiter and Saturn (Malhotra et al. 1989; Minton & Malhotra 2011). The vertical black-dotted line shows the location of this 2:1 mean-motion resonance and the semi-major axis of the inner Jupiter mass planetary companion is shown by the horizontal gray line.

location of the intersection with the precession rate of a test particle. The precession frequency of the test particle and the outer companion's eigenfrequency were both calculated by including the inner and outer companions. We included a correction due to the near 2:1 mean-motion resonance between the two companions (Malhotra et al. 1989; Minton & Malhotra 2011).

Figure 5.5 shows the location of the ν_6 secular resonance for three different architectures as a function of planetary companion semi-major axis with a variety of planetary masses for the outer companion that include 1.0 Saturn mass (${\rm M_S}$), 1.0 Jupiter mass (${\rm M_J}$), $5.0\,{\rm M_J}$, and $10.0\,{\rm M_J}$. We consider the case where the planetary companion is orbiting a $0.5\,{\rm M}_\odot$ white dwarf. The inner and outer companion's orbits expand adiabatically in response to the amount of stellar mass loss. For comparison, the inner planetary companion's semi-major axis is denoted in Fig. 5.5 by the horizontal gray line. If we assume that the asteroid belt has the same adiabatic location, the more

massive the planetary companion, the wider the companion orbital separation that is needed to pollute the atmospheres of white dwarfs.

There are many known planetary system architectures in the Kepler data (Borucki et al. 2010; 2011; Batalha et al. 2013). Given that white dwarf pollution occurs in vastly different planetary systems than our Solar System, these results may have implications on white dwarf pollution in a wide range of exo-planetary architectures.

Roughly 50% of stars in the Milky Way are in binary systems. Many polluted white dwarfs are also observed in binary systems (Zuckerman et al. 2003). The proposed theoretical models for white dwarf pollution in binaries include wide-binary perturbations (Bonsor & Veras 2015) and Kozai-Lidov oscillations (Hamers & Portegies Zwart 2016; Petrovich & Muñoz 2017). Here we consider closer binaries that are close to coplanar to the planetary system.

To identify how the secular resonance operates in a binary system, we use our analytic model described in Chapter. 2. We replace the outer planetary companion with a stellar companion. In Fig. 5.6 we vary the mass and semi-major axis of the companion star for a $0.5\,\mathrm{M}_{\odot}$ white dwarf and calculate the location of the resulting secular resonance for three different semi-major axis values of the inner Jupiter mass planet. In Fig. 5.6, the location of the inner planet is $6.0\,\mathrm{AU}$ (left panel), $10.4\,\mathrm{AU}$ (middle panel), and $30\,\mathrm{AU}$ (right panel).

In each case, we vary the mass of the companion star as listed: $0.5\,\mathrm{M}_{\odot}$ (solid line), $1.0\,\mathrm{M}_{\odot}$ (dashed), $5.0\,\mathrm{M}_{\odot}$ (dotted) and $10.0\,\mathrm{M}_{\odot}$ (dot-dashed). The middle panel corresponds to Jupiter at $5.2\mathrm{AU}$ initially. In each panel, as the mass of the stellar companion increases, the location of the secular resonance can exist at a wider binary separations. Since these represent theoretical models only, we do not assume a definitive location of an exo-asteroid belt. These models demonstrate that a wide variety of binary configurations may produce white dwarf pollution. This pollution

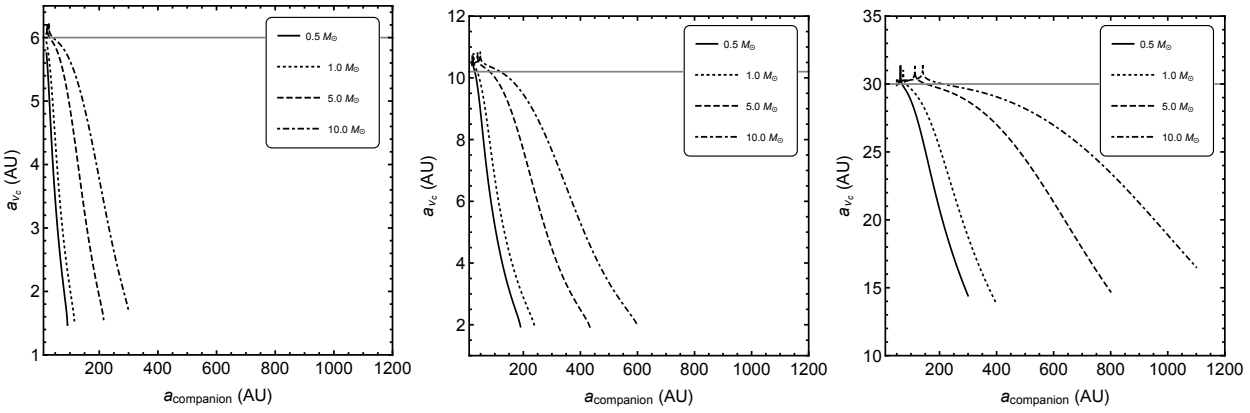

Figure 5.6: The location of the companion (ν_c) secular resonance as a function of the orbital separation of the stellar companion for various stellar companion masses. We also vary the semi-major axis of the inner planetary companion as follows: $6\,\mathrm{AU}$ (left panel), $10.4\,\mathrm{AU}$ (middle panel), and $30\,\mathrm{AU}$ (right panel). The masses that were modeled include $0.5\,\mathrm{M}_\odot$ (solid), $1.0\,\mathrm{M}_\odot$ (dotted), $5.0\,\mathrm{M}_\odot$ (dashed), and $10.0\,\mathrm{M}_\odot$ (dot-dashed). The companion star is orbiting a $0.5\,\mathrm{M}_\odot$ white dwarf with a Jupiter-mass planet with a semi-major axis shown by the horizontal gray line.

mechanism (of secular perturbations) is not able to model pollution of white dwarfs located within wide-binaries ($a_{\rm binary} > 1000\,\mathrm{AU}$). Depending on the semi-major axis of the giant planet, this mechanism can support WD pollution located in binaries with a binary separation $< 1000\,\mathrm{AU}$.

These analytic models may provide a pollution mechanism of white dwarf atmospheres for a variety of planetary configurations. These models suggest that pollution via secular resonances is somewhat robust, since these models need two companions plus engulfment of a terrestrial planet.

CHAPTER 6

CONCLUSION

We found that the ν_6 resonance may play an important role in producing asteroid collisions with terrestrial planets in the inner parts of a planetary system which corresponds to previous works (Morbidelli et al. 1994; Gladman et al. 1997; Bottke et al. 2000; Ito & Malhotra 2006; Minton & Malhotra 2011) an asteroid belt and two giant planets, in this order in terms of their separation from the central star. We have explored how the planetary system architecture affects the location and width of the ν_6 resonance and how this in turn affects the number of asteroid collisions with the Earth. Since super–Earths are common in the inner regions of exoplanetary systems we first considered their influence. A super–Earth with with a mass of around $10\,\mathrm{M}_\oplus$ at an orbital radius greater than about $> 0.7\,\mathrm{AU}$ may significantly affect the number and rate of asteroid collisions on the Earth. A super-Earth interior to the Earth's orbit increases the number of asteroid collisions with the Earth, while a super–Earth between the Earth and the asteroid belt decreases the number of asteroid collisions. Furthermore, we find that increasing the mass of Saturn increases the number of asteroid collisions. Changing the location of Saturn generally leads to a significant decrease in the number of asteroid collisions.

Schlichting et al. (2012) proposed that additional collisions from a residual planetesimal population is needed to damp the high eccentricities and inclinations of terrestrial planets during the late stages of planet formation. This damping mechanism would allow terrestrial planets to evolve onto circular and coplanar orbits. Geochemical evidence suggests that the Earth accreted roughly 0.3%–

0.7% of its total mass in the form of chondritic material during the late stages of planet formation (Walker 2009). If these series of events are indeed true, this implies that asteroid collisions may have an important effect on determining the habitability of planets located in exoplanetary systems, which would prompt these results in this work to be potentially very significant. In particular, and to end on a speculative note, Martin & Livio (2016) proposed a model in which super–Earths did form in the inner parts of the solar system, but then migrated into the Sun. This chain of events, if it had indeed happened, could have helped regulate asteroid impacts to a rate and pattern conducive to the emergence of life on Earth.

We have found that secular resonances, in particular the ν_6 resonance, lead to polluted white dwarfs. In the solar system, if the Earth becomes engulfed by the Sun as it leaves the main–sequence, the ν_6 resonance shifts outward, causing previously stable asteroids to undergo secular resonant perturbations that lead to tidal disruptions close to the white dwarf and the white dwarf will be polluted. This mechanism can lead to white dwarf pollution for a large range of planetary system parameters including systems with two giant planets, or one planet and a binary star companion.

Unlike mean-motion resonances, the location of secular resonance do not behave in a linear fashion. Thus, a larger amount of previously stable asteroids become eccentric by secular perturbations and then become tidally disrupted by the white dwarf, leading to metal-rich material accreting onto the white dwarf. We expect the process of asteroid perturbations by secular resonances to last much longer than the white dwarf cooling age given a massive enough asteroid belt. Debes et al. (2012) found that the current mass of the asteroid belt would need to increase $10^2 - 10^4$ times in order for a sufficient amount of material to be accreted by the white dwarf. Frewen & Hansen (2014) later found that their model required a planetesimal disk to be a few

thousand times larger than the asteroid belt, which matches the results from Debes et al. (2012).

Despite that the Solar System will not have a polluted white dwarf due to asteroidal accretion, the analytical and numerical models used within this work may be viable in explaining white dwarf pollution in exoplanetary systems. There is strong evidence that there may not be just one mechanism that produces white dwarf pollution. Theoretically, our secular resonance model and Debes et al. (2012) mean-motion resonance model would occur in a synergistic manner, allowing a larger fraction of asteroids to become tidally disrupted, but we expect that the secular perturbations last longer than mean-motion perturbations.

BIBLIOGRAPHY

Aannestad, P. A., Kenyon, S. J., Hammond, G. L., & Sion, E. M. 1993, AJ, 105, 1033

Adams, F. C. & Bloch, A. M. 2013, ApJ, 777, L30

Agnor, C. B. & Ward, W. R. 2002, ApJ, 567, 579

Alexander, R. D., Clarke, C. J., & Pringle, J. E. 2006, MNRAS, 369, 229

Armitage, P. J. 2013, Astrophysics of Planet Formation

Artymowicz, P. 1993, ApJ, 419, 166

Baines, E. K., White, R. J., Huber, D., Jones, J., Boyajian, T., McAlister, H. A., ten Brummelaar, T. A., Turner, N. H., Sturmann, J., Sturmann, L., Goldfinger, P. J., Farrington, C. D., Riedel, A. R., Ireland, M., von Braun, K., & Ridgway, S. T. 2012, ApJ, 761, 57

Barstow, M. A., Barstow, J. K., Casewell, S. L., Holberg, J. B., & Hubeny, I. 2014, MNRAS, 440, 1607

Batalha, N. M., Rowe, J. F., Bryson, S. T., Barclay, T., Burke, C. J., Caldwell, D. A., Christiansen, J. L., Mullally, F., Thompson, S. E., Brown, T. M., Dupree, A. K., Fabrycky, D. C., Ford, E. B., Fortney, J. J., Gilliland, R. L., Isaacson, H., Latham, D. W., Marcy, G. W., Quinn, S. N., Ragozzine, D., Shporer, A., Borucki, W. J., Ciardi, D. R., Gautier, III, T. N., Haas, M. R., Jenkins, J. M., Koch, D. G., Lissauer, J. J., Rapin, W., Basri, G. S., Boss, A. P., Buchhave, L. A., Carter, J. A., Charbonneau, D., Christensen-Dalsgaard, J., Clarke, B. D., Cochran, W. D., Demory, B.-O., Desert, J.-M., Devore, E., Doyle, L. R., Esquerdo, G. A., Everett, M., Fressin, F., Geary, J. C., Girouard, F. R., Gould, A., Hall, J. R., Holman, M. J., Howard, A. W., Howell, S. B., Ibrahim, K. A., Kinemuchi, K., Kjeldsen, H., Klaus, T. C., Li, J., Lucas, P. W., Meibom, S., Morris, R. L., Prša, A., Quintana, E., Sanderfer, D. T., Sasselov, D., Seader, S. E., Smith, J. C., Steffen, J. H., Still, M., Stumpe, M. C., Tarter, J. C., Tenenbaum, P., Torres, G., Twicken, J. D., Uddin, K., Van Cleve, J., Walkowicz, L., & Welsh, W. F. 2013, ApJS, 204, 24

Bear, E. & Soker, N. 2013, New Astronomy, 19, 56

Bonsor, A. & Veras, D. 2015, MNRAS, 454, 53

Borucki, W. J., Koch, D., Basri, G., Batalha, N., Brown, T., Caldwell, D., Caldwell, J., Christensen-Dalsgaard, J., Cochran, W. D., DeVore, E., Dunham, E. W., Dupree, A. K., Gautier, T. N., Geary, J. C., Gilliland, R., Gould, A., Howell, S. B., Jenkins, J. M., Kondo, Y., Latham, D. W., Marcy, G. W., Meibom, S., Kjeldsen, H., Lissauer, J. J., Monet, D. G., Morrison, D., Sasselov, D., Tarter, J., Boss, A., Brownlee, D., Owen, T., Buzasi, D., Charbonneau, D., Doyle, L., Fortney, J., Ford, E. B., Holman, M. J., Seager, S., Steffen, J. H., Welsh, W. F., Rowe, J., Anderson, H., Buchhave, L., Ciardi, D., Walkowicz, L., Sherry, W., Horch, E., Isaacson, H., Everett, M. E., Fischer, D., Torres, G., Johnson, J. A., Endl, M., MacQueen, P., Bryson, S. T., Dotson, J., Haas, M., Kolodziejczak, J., Van Cleve, J., Chandrasekaran, H., Twicken, J. D., Quintana, E. V., Clarke, B. D., Allen, C., Li, J., Wu, H., Tenenbaum, P., Verner, E., Bruhweiler, F., Barnes, J., & Prsa, A. 2010, Science, 327, 977

Borucki, W. J., Koch, D. G., Basri, G., Batalha, N., Brown, T. M., Bryson, S. T., Caldwell, D., Christensen-Dalsgaard, J., Cochran, W. D., DeVore, E., Dunham, E. W., Gautier, III, T. N., Geary, J. C., Gilliland, R., Gould, A., Howell, S. B., Jenkins, J. M., Latham, D. W., Lissauer,

J. J., Marcy, G. W., Rowe, J., Sasselov, D., Boss, A., Charbonneau, D., Ciardi, D., Doyle, L., Dupree, A. K., Ford, E. B., Fortney, J., Holman, M. J., Seager, S., Steffen, J. H., Tarter, J., Welsh, W. F., Allen, C., Buchhave, L. A., Christiansen, J. L., Clarke, B. D., Das, S., Désert, J.-M., Endl, M., Fabrycky, D., Fressin, F., Haas, M., Horch, E., Howard, A., Isaacson, H., Kjeldsen, H., Kolodziejczak, J., Kulesa, C., Li, J., Lucas, P. W., Machalek, P., McCarthy, D., MacQueen, P., Meibom, S., Miquel, T., Prsa, A., Quinn, S. N., Quintana, E. V., Ragozzine, D., Sherry, W., Shporer, A., Tenenbaum, P., Torres, G., Twicken, J. D., Van Cleve, J., Walkowicz, L., Witteborn, F. C., & Still, M. 2011, ApJ, 736, 19

Bottke, W. F., Morbidelli, A., Jedicke, R., Petit, J.-M., Levison, H. F., Michel, P., & Metcalfe, T. S. 2002, Icarus, 156, 399

Bottke, W. F., Vokrouhlický, D., Minton, D., Nesvorný, D., Morbidelli, A., Brasser, R., Simonson, B., & Levison, H. F. 2012, Nature, 485, 78

Bottke, Jr., W. F., Rubincam, D. P., & Burns, J. A. 2000, Icarus, 145, 301

Brouwer, D. & van Woerkom, A. J. J. 1950, Astronomical papers prepared for the use of the American ephemeris and nautical almanac, v.13, pt.2, Washington : U.S. Govt. Print. Off., 1950., p. 81-107 : 29 cm., 13, 81

Brož, M. & Vokrouhlický, D. 2008, MNRAS, 390, 715

Brown, J. C., Veras, D., & Gänsicke, B. T. 2017, MNRAS, 468, 1575

Caiazzo, I. & Heyl, J. S. 2017, ArXiv e-prints

Canup, R. M. 2012, Science, 338, 1052

Canup, R. M. & Asphaug, E. 2001, Nature, 412, 708

Castillo-Rogez, J. C., Matson, D. L., Kargel, J. S., Vance, S. D., & Johnson, T. V. 2008, in Lunar and Planetary Science Conference, Vol. 39, Lunar and Planetary Science Conference, 2461

Chambers, J. E. 1999, MNRAS, 304, 793

Chatterjee, S., Ford, E. B., Matsumura, S., & Rasio, F. A. 2008, ApJ, 686, 580

Chiang, E. & Laughlin, G. 2013, MNRAS, 431, 3444

Chrenko, O., Brož, M., Nesvorný, D., Tsiganis, K., & Skoulidou, D. K. 2015, MNRAS, 451, 2399

Cottrell, P. L. & Greenstein, J. L. 1980, ApJ, 242, 195

Cronin, J. R. & Pizzarello, S. 1983, Advances in Space Research, 3, 5

Davidsson, B. J. R. 1999, Icarus, 142, 525

Dawson, R. I. & Murray-Clay, R. A. 2013, ApJ, 767, L24

Debes, J. H., Walsh, K. J., & Stark, C. 2012, ApJ, 747, 148

Dermott, S. F. & Murray, C. D. 1983, Nature, 301, 201

Dohnanyi, J. S. 1969, J. Geophys. Res., 74, 2531

Duncan, M. J. & Lissauer, J. J. 1998, Icarus, 134, 303

Falcon, R. E., Winget, D. E., Montgomery, M. H., & Williams, K. A. 2010, ApJ, 712, 585

Farihi, J. 2016, New Astronomy Reviews, 71, 9

Farihi, J., Barstow, M. A., Redfield, S., Dufour, P., & Hambly, N. C. 2010a, MNRAS, 404, 2123

Farihi, J., Jura, M., Lee, J.-E., & Zuckerman, B. 2010b, ApJ, 714, 1386

Farihi, J., Jura, M., & Zuckerman, B. 2009, ApJ, 694, 805

Fernandez, J. A. & Ip, W.-H. 1984, Icarus, 58, 109

Fernández, J. A. & Ip, W.-H. 1996, Planet. Space Sci., 44, 431

Fontaine, G., Brassard, P., & Bergeron, P. 2001, PASP, 113, 409

Fontaine, G. & Michaud, G. 1979, ApJ, 231, 826

Ford, E. B. & Rasio, F. A. 2008, ApJ, 686, 621

Frewen, S. F. N. & Hansen, B. M. S. 2014, MNRAS, 439, 2442
Froeschle, C. & Scholl, H. 1986, A&A, 166, 326
Gänsicke, B. T., Marsh, T. R., Southworth, J., & Rebassa-Mansergas, A. 2006, Science, 314, 1908
Genda, H. & Ikoma, M. 2008, Icarus, 194, 42
Gladman, B. 1993, Icarus, 106, 247
Gladman, B. J., Migliorini, F., Morbidelli, A., Zappala, V., Michel, P., Cellino, A., Froeschle, C., Levison, H. F., Bailey, M., & Duncan, M. 1997, Science, 277, 197
Gomes, R. S., Morbidelli, A., & Levison, H. F. 2004, Icarus, 170, 492
Goździewski, K. & Migaszewski, C. 2014, MNRAS, 440, 3140
Granvik, M., Morbidelli, A., Vokrouhlický, D., Bottke, W. F., Nesvorný, D., & Jedicke, R. 2017, A&A, 598, A52
Haisch, Jr., K. E., Lada, E. A., & Lada, C. J. 2001, ApJ, 553, L153
Hamers, A. S. & Portegies Zwart, S. F. 2016, MNRAS, 462, L84
Han, E., Wang, S. X., Wright, J. T., Feng, Y. K., Zhao, M., Fakhouri, O., Brown, J. I., & Hancock, C. 2014, PASP, 126, 827
Hansen, B. M. S. & Murray, N. 2013, ApJ, 775, 53
Horner, J. & Jones, B. W. 2008, International Journal of Astrobiology, 7, 251
—. 2012, International Journal of Astrobiology, 11, 147
Houtkooper, J. M. 2011, Planet. Space Sci., 59, 1107
Ito, T. & Malhotra, R. 2006, Advances in Space Research, 38, 817
Ito, T. & Tanikawa, K. 1999, Icarus, 139, 336
—. 2002, MNRAS, 336, 483
Izidoro, A., Raymond, S. N., Pierens, A., Morbidelli, A., Winter, O. C., & Nesvorny‘, D. 2016, ApJ, 833, 40
Jura, M. 2003, ApJ, 584, L91
—. 2006, ApJ, 653, 613
Jura, M., Muno, M. P., Farihi, J., & Zuckerman, B. 2009, ApJ, 699, 1473
Kilic, M. & Redfield, S. 2007, ApJ, 660, 641
Kilic, M., von Hippel, T., Leggett, S. K., & Winget, D. E. 2006, ApJ, 646, 474
Klein, B., Jura, M., Koester, D., Zuckerman, B., & Melis, C. 2010, ApJ, 709, 950
Koester, D. 2009, A&A, 498, 517
Koester, D., Gänsicke, B. T., & Farihi, J. 2014, A&A, 566, A34
Koester, D., Provencal, J., & Shipman, H. L. 1997, A&A, 320, L57
Koester, D., Weidemann, V., Zeidler, E. M., & Vauclair, G. 1982, A&A, 113, L13
Koester, D. & Wilken, D. 2006, A&A, 453, 1051
Kominami, J. & Ida, S. 2002, Icarus, 157, 43
Kozai, Y. 1962, AJ, 67, 591
Krasinsky, G. A., Pitjeva, E. V., Vasilyev, M. V., & Yagudina, E. I. 2002, Icarus, 158, 98
Lacombe, P., Wesemael, F., Fontaine, G., & Liebert, J. 1983, ApJ, 272, 660
Lecar, M. & Franklin, F. 1997, Icarus, 129, 134
Lecar, M., Podolak, M., Sasselov, D., & Chiang, E. 2006, ApJ, 640, 1115
Lidov, M. L. 1962, Planet. Space Sci., 9, 719
Liebert, J., Bergeron, P., & Holberg, J. B. 2005, ApJS, 156, 47
Lissauer, J. J., Ragozzine, D., Fabrycky, D. C., Steffen, J. H., Ford, E. B., Jenkins, J. M., Shporer, A., Holman, M. J., Rowe, J. F., Quintana, E. V., Batalha, N. M., Borucki, W. J., Bryson, S. T.,

Caldwell, D. A., Carter, J. A., Ciardi, D., Dunham, E. W., Fortney, J. J., Gautier, III, T. N., Howell, S. B., Koch, D. G., Latham, D. W., Marcy, G. W., Morehead, R. C., & Sasselov, D. 2011, ApJS, 197, 8
Malhotra, R. 1999, Nature, 402, 599
Malhotra, R. 2012, Encyclopedia of Life Support Systems by UNESCO, 6, 55
Malhotra, R., Fox, K., Murray, C. D., & Nicholson, P. D. 1989, A&A, 221, 348
Maoz, D. 2016, Astrophysics in a Nutshell
Marois, C., Zuckerman, B., Konopacky, Q. M., Macintosh, B., & Barman, T. 2010, Nature, 468, 1080
Martin, R. G. & Livio, M. 2013, MNRAS, 434, 633
—. 2015, ApJ, 810, 105
—. 2016, ApJ, 822, 90
Martin, R. G., Lubow, S. H., Nixon, C., & Armitage, P. J. 2016, MNRAS, 458, 4345
McDonald, I. & Zijlstra, A. A. 2015, MNRAS, 448, 502
Melis, C. & Dufour, P. 2017, ApJ, 834, 1
Melis, C., Jura, M., Albert, L., Klein, B., & Zuckerman, B. 2010, ApJ, 722, 1078
Michtchenko, T. A. & Ferraz-Mello, S. 2001, Icarus, 149, 357
Minton, D. A. & Malhotra, R. 2010, Icarus, 207, 744
—. 2011, ApJ, 732, 53
Moons, M. 1996, Celestial Mechanics and Dynamical Astronomy, 65, 175
Morales, F. Y., Rieke, G. H., Werner, M. W., Bryden, G., Stapelfeldt, K. R., & Su, K. Y. L. 2011, ApJ, 730, L29
Morbidelli, A., Chambers, J., Lunine, J. I., Petit, J. M., Robert, F., Valsecchi, G. B., & Cyr, K. E. 2000, Meteoritics and Planetary Science, 35, 1309
Morbidelli, A. & Gladman, B. 1998, Meteoritics and Planetary Science, 33, 999
Morbidelli, A., Gonczi, R., Froeschle, C., & Farinella, P. 1994, A&A, 282, 955
Morbidelli, A. & Nesvorný, D. 1999, Icarus, 139, 295
Morbidelli, A., Zappala, V., Moons, M., Cellino, A., & Gonczi, R. 1995, Icarus, 118, 132
Moro-Martín, A., Malhotra, R., Bryden, G., Rieke, G. H., Su, K. Y. L., Beichman, C. A., & Lawler, S. M. 2010, ApJ, 717, 1123
Morrison, S. & Malhotra, R. 2015, ApJ, 799, 41
Morton, T. D. & Winn, J. N. 2014, ApJ, 796, 47
Murray, C. D. & Dermott, S. F. 2000, Solar System Dynamics
Murray, N. & Holman, M. 1997, AJ, 114, 1246
—. 1999, Science, 283, 1877
Mustill, A. J. & Villaver, E. 2012, ApJ, 761, 121
Nesvorný, D. & Morbidelli, A. 1998, AJ, 116, 3029
O'Brien, D. P., Morbidelli, A., & Bottke, W. F. 2007, Icarus, 191, 434
Paquette, C., Pelletier, C., Fontaine, G., & Michaud, G. 1986, ApJS, 61, 197
Payne, M. J., Veras, D., Gänsicke, B. T., & Holman, M. J. 2017, MNRAS, 464, 2557
Payne, M. J., Veras, D., Holman, M. J., & Gänsicke, B. T. 2016, MNRAS, 457, 217
Petit, J.-M., Morbidelli, A., & Chambers, J. 2001, Icarus, 153, 338
Petrovich, C. & Muñoz, D. J. 2017, ApJ, 834, 116
Raymond, S. N., O'Brien, D. P., Morbidelli, A., & Kaib, N. A. 2009, Icarus, 203, 644
Raymond, S. N., Quinn, T., & Lunine, J. I. 2007, Astrobiology, 7, 66

Reimers, D. 1977, A&A, 54, 485
Rosenfield, P., Marigo, P., Girardi, L., Dalcanton, J. J., Bressan, A., Gullieuszik, M., Weisz, D., Williams, B. F., Dolphin, A., & Aringer, B. 2014, ApJ, 790, 22
Rosenfield, P., Marigo, P., Girardi, L., Dalcanton, J. J., Bressan, A., Williams, B. F., & Dolphin, A. 2016, ApJ, 822, 73
Sackmann, I.-J., Boothroyd, A. I., & Kraemer, K. E. 1993, ApJ, 418, 457
Schlichting, H. E., Warren, P. H., & Yin, Q.-Z. 2012, ApJ, 752, 8
Schröder, K.-P. & Connon Smith, R. 2008, MNRAS, 386, 155
Siess, L. & Livio, M. 1999, MNRAS, 308, 1133
Smallwood, J. S., Martin, R. G., Lepp, S., & Livio, M. 2017, MNRAS, submitted
Strom, R. G., Malhotra, R., Ito, T., Yoshida, F., & Kring, D. A. 2005, Science, 309, 1847
Takeda, G. & Rasio, F. A. 2005, ApJ, 627, 1001
Tremblay, P.-E., Cummings, J., Kalirai, J. S., Gänsicke, B. T., Gentile-Fusillo, N., & Raddi, R. 2016, MNRAS, 461, 2100
Valencia, D., Sasselov, D. D., & O'Connell, R. J. 2007, ApJ, 665, 1413
Vauclair, G., Vauclair, S., & Greenstein, J. L. 1979, A&A, 80, 79
Vennes, S., Kawka, A., & Németh, P. 2010, MNRAS, 404, L40
Veras, D., Hadjidemetriou, J. D., & Tout, C. A. 2013, MNRAS, 435, 2416
Villaver, E. & Livio, M. 2007, ApJ, 661, 1192
—. 2009, ApJ, 705, L81
Villaver, E., Livio, M., Mustill, A. J., & Siess, L. 2014, ApJ, 794, 3
von Hippel, T., Kuchner, M. J., Kilic, M., Mullally, F., & Reach, W. T. 2007, ApJ, 662, 544
Vrbik, J. 1996, Journal of Physics A Mathematical General, 29, 3311
Walker, R. J. 2009, Chemie der Erde / Geochemistry, 69, 101
Ward, W. R. 1989, ApJ, 345, L99
—. 1993, Icarus, 106, 274
Willbold, M., Elliott, T., & Moorbath, S. 2011, Nature, 477, 195
Wu, Y. & Murray, N. 2003, ApJ, 589, 605
Wyatt, M. C. 2003, ApJ, 598, 1321
Yoshikawa, M. 1987, Celestial Mechanics, 40, 233
Zeidler-K.T., E.-M., Weidemann, V., & Koester, D. 1986, A&A, 155, 356
Zuckerman, B., Koester, D., Reid, I. N., & Hünsch, M. 2003, ApJ, 596, 477
Zuckerman, B., Melis, C., Klein, B., Koester, D., & Jura, M. 2010, ApJ, 722, 725

CURRICULUM VITAE

Jeremy Smallwood

Department of Physics and Astronomy
University of Nevada, Las Vegas
Las Vegas
NV 89154, USA

smallj2@unlv.nevada.edu

EDUCATION

Aug 2015 - present	**MS in Astronomy** University of Nevada, Las Vegas
Aug 2010 - May 2015	**BA Astrophysics** Baylor University, Waco, Texas

WORK EXPERIENNCE

Aug 2016 - May 2017	Graduate Assistant Department of Physics and Astronomy, University of Nevada, Las Vegas
Jan 2015 - May 2015	Teaching Assistant for Astronomy Laboratory Department of Physics, Baylor University
Jan 2015 - May 2015	Teaching Assistant for Physics of Sound and Acoustics Laboratory Department of Physics, Baylor University
Aug 2014 - Dec 2014	Teaching Assistant for Partial Differential Equations Department of Mathematics, Baylor University
Aug 2012 - May 2013	Supplemental Instructor in Chemistry Department of Chemistry, Baylor University

PUBLICATIONS

1. Asteroid impacts on terrestrial planets: The effects of super–Earth and the role of the ν_6 resonance
   Smallwood J. L., Martin R. G., Lepp S., Livio M., MNRAS, submitted

2. White dwarf pollution by asteroids from secular resonances
   Smallwood J. L., Martin R. G., Livio M., MNRAS, to be submitted